

# Using crystal lattice distortion data for geological investigations: the Weighted Burgers Vector method

John Wheeler<sup>1</sup>, Sandra Piazzolo<sup>2</sup>, David John Prior<sup>3</sup>, Patrick W Trimby<sup>4</sup>, and Jacob A Tielke<sup>5</sup>

<sup>1</sup>University of Liverpool

<sup>2</sup>School of Earth and Environment, The University of Leeds

<sup>3</sup>University of Otago

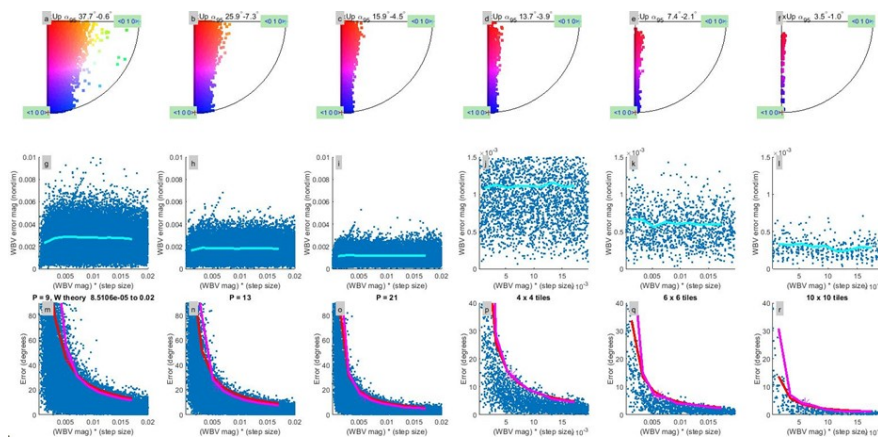
<sup>4</sup>Oxford Instruments

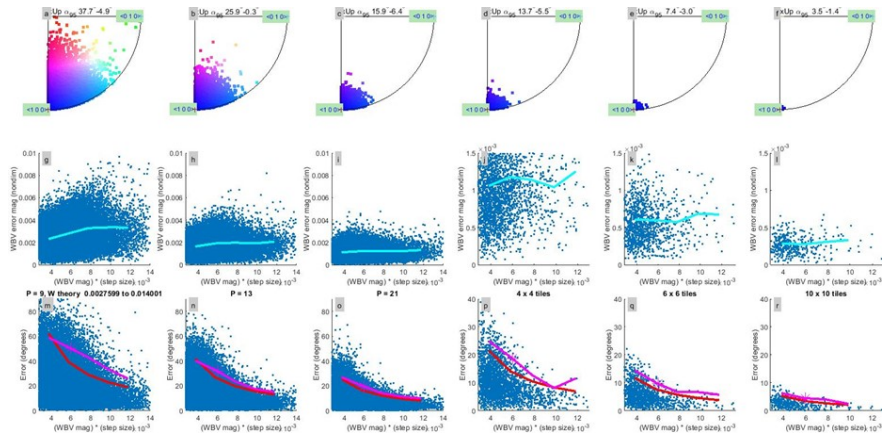
<sup>5</sup>Lamont-Doherty Earth Observatory

May 22, 2023

## Abstract

Distorted crystals carry useful information on processes involved in their formation, deformation and growth. The distortions are accommodated by geometrically necessary dislocations, and therefore characterising those dislocations is an informative task, to assist in, for example, deducing the slip systems that produced the dislocations. Electron Backscatter Diffraction (EBSD) allows detailed quantification of distorted crystal orientations and we summarise here a method for extracting information on dislocations from such data. The Weighted Burgers Vector (WBV) method calculates a vector at each point on an EBSD map, or an average over a region. The vector is a weighted average of the Burgers vectors of dislocation lines intersecting the map surface. It is weighted towards dislocation lines at a high angle to the map but that can be accounted for in interpretation. The method is fast and does not involve specific assumptions about dislocation types. It can be used, with care, to analyse subgrain walls (sharp orientation changes) as well as gradational orientation changes within individual grains. We describe new and published examples of the use of the technique to illustrate its potential; case studies to date mainly use the WBV direction not the magnitude. EBSD orientation data have angular errors, and so does the WBV. We present an analysis of these angular errors, showing there is a trade-off between directional accuracy and area sampled. In summary the technique is fast, free from assumptions, and errors can be taken into account to allow testing of hypotheses about dislocation types.





## Using crystal lattice distortion data for geological investigations: the Weighted Burgers Vector method

J. Wheeler<sup>1</sup>, S. Piazzolo<sup>2</sup>, D. J. Prior<sup>3</sup>, P. W. Trimby<sup>4</sup> and J. A. Tielke<sup>5</sup>

<sup>1</sup>Department of Earth, Ocean, and Ecological Sciences, University of Liverpool, 4 Brownlow Street, Liverpool, L69 3GP, UK

<sup>2</sup>University of Leeds, School of Earth & Environment, Leeds LS2 9JT, UK

<sup>3</sup>Department of Geology, University of Otago, Dunedin, New Zealand

<sup>4</sup>Oxford Instruments Nanoanalysis, High Wycombe, Bucks, England

<sup>5</sup>Lamont-Doherty Earth Observatory of Columbia University, Palisades, NY, USA

### Abstract

Distorted crystals carry useful information on processes involved in their formation, deformation and growth. The distortions are accommodated by geometrically necessary dislocations, and therefore characterising those dislocations is an informative task, to assist in, for example, deducing the slip systems that produced the dislocations. Electron Backscatter Diffraction (EBSD) allows detailed quantification of distorted crystal orientations and we summarise here a method for extracting information on dislocations from such data. The Weighted Burgers Vector (WBV) method calculates a vector at each point on an EBSD map, or an average over a region. The vector is a weighted average of the Burgers vectors of dislocation lines intersecting the map surface. It is weighted towards dislocation lines at a high angle to the map but that can be accounted for in interpretation. The method is fast and does not involve specific assumptions about dislocation types. It can be used, with care, to analyse subgrain walls (sharp orientation changes) as well as gradational orientation changes within individual grains. We describe new and published examples of the use of the technique to illustrate its potential; case studies to date mainly use the WBV direction not the magnitude. EBSD orientation data have angular errors, and so does the WBV. We present an analysis of these angular errors, showing there is a trade-off between directional accuracy and area sampled. In summary the technique is fast, free from assumptions, and errors can be taken into account to allow testing of hypotheses about dislocation types.

### Plain Language Summary

Rocks, and also metals and ceramics, are made of interlocking crystals. Crystals are defined as having regular atomic structures, but growth problems or deformation can give rise to linear imperfections in the regular arrangements. These lines (dislocations) carry valuable information about deformation or growth but are difficult to see. However, when there are huge numbers distributed through the crystal, it may be visibly distorted: the atomic sheets, ideally planar, are curved. An electron microscopy technique enables us to measure the orientations of atomic sheets. In this contribution we describe a mathematical method which calculates the “offsets” in atomic structure, related to dislocations, from orientation measurements. These “Burgers vectors” carry key information about how atoms have slipped past each other during deformation, a process which operates on the scale of the whole Earth. The calculation method gives us information on these vectors quickly and without having to make prior assumptions about what vectors to expect. Because orientation measurements

have errors, the calculated vectors have errors, and we show how to estimate these. We give examples showing how useful such calculations are, particularly in understanding how crystals – and hence the Earth - deform.

## Key points

This method allows calculation of information about Burgers vectors, without prior assumptions, from crystal orientation measurements

Errors in the calculated vectors due to orientation measurement errors are quantified

## 1. Introduction

Microstructures are crucial indicators of processes which have affected rocks. Dislocations provide evidence for how and under what conditions individual grains have deformed, or may be growth defects indicating growth conditions. If dislocations are due to deformation their Burgers vectors may help constrain the style or conditions of deformation. Individual dislocations give a lattice extra energy, so the density of dislocations is needed to estimate this on a volumetric basis. This plastic strain energy provides a driving force for recrystallization in deformed rocks (Drury and Urai, 1990). TEM is the standard method to image individual dislocations, a procedure which can be laborious and will characterise just a tiny fraction of the microstructure, leaving doubts as to how representative it is. In contrast intracrystalline distortions may be optically visible and can be quickly characterised by EBSD mapping over large regions. Such distortions, regardless of cause, must be accommodated by geometrically necessary dislocations (GNDs) (Ashby, 1970) and hence give indirect information on dislocation content. In principle it would be useful to constrain *directional* (lines, Burgers vectors) and *magnitude* (dislocation density) information from EBSD data: examples of approaches follow.

If distortion is due to deformation by dislocation motion it can in principle be used to constrain active slip systems (hence deformation conditions) using directional information. Such studies have often focussed on subgrain walls (in essence, localised sharp distortions). For example Lloyd (2002) argues that subgrain wall traces and misorientation axes in quartz can be used to deduce slip systems, though assumptions about “pure” tilt or twist nature of boundaries are needed. Wieser et al. (2020) applied a modified approach to olivine, incorporating subgrain wall traces with information from the method of Wheeler et al. (2009). The latter, the Weighted Burgers Vector (WBV) method, is what we discuss in this contribution. Distortion in olivine can be used to deduce slip systems, with calculations assuming that the net dislocation energy is minimised with respect to all possible combinations of dislocation lines and Burgers vectors (Lopez-Sanchez et al., 2021; Wallis et al., 2016; Wallis et al., 2019b). Distortion magnitude information can be quantified using for example “local misorientation” though the link to actual dislocation densities is not straightforward to make. For example Timms et al. (2012) use local misorientation maps to give an overview of the heterogeneous distortion in shocked zircon crystals.

If distortion is due to growth, or is postulated to be, then purely geometric analyses can be applied as they would be to deformed crystals but any extra assumptions must be evaluated with care. Spruzeniece et al. (2017) quantified crystal distortions in KBr-KCl solid solution grown in a stress-free environment: these are due to growth not deformation. Gardner et al.

(2021) examined natural distorted albite and showed that some subgrain walls contain dislocations with Burgers vectors with  $\langle 010 \rangle$  components. There are no known slip systems with such Burgers vectors, so the subgrain walls were diagnosed as growth defects.

The methods in these and many other papers using EBSD to analyse distortions include various assumptions, both in manual processes (e.g. selecting straight segments of boundary traces) and in automatic calculations (e.g. assumptions about allowed slip systems and dislocation energy minimisation). It is generally not clear how errors in EBSD orientation measurements affect deductions, and some methods are slow if they are manual or compute intensive. Methods using boundary trace analysis cannot be applied to smooth, distributed distortions because there are no discrete boundaries. Overall, the methods have diverse strengths and weaknesses.

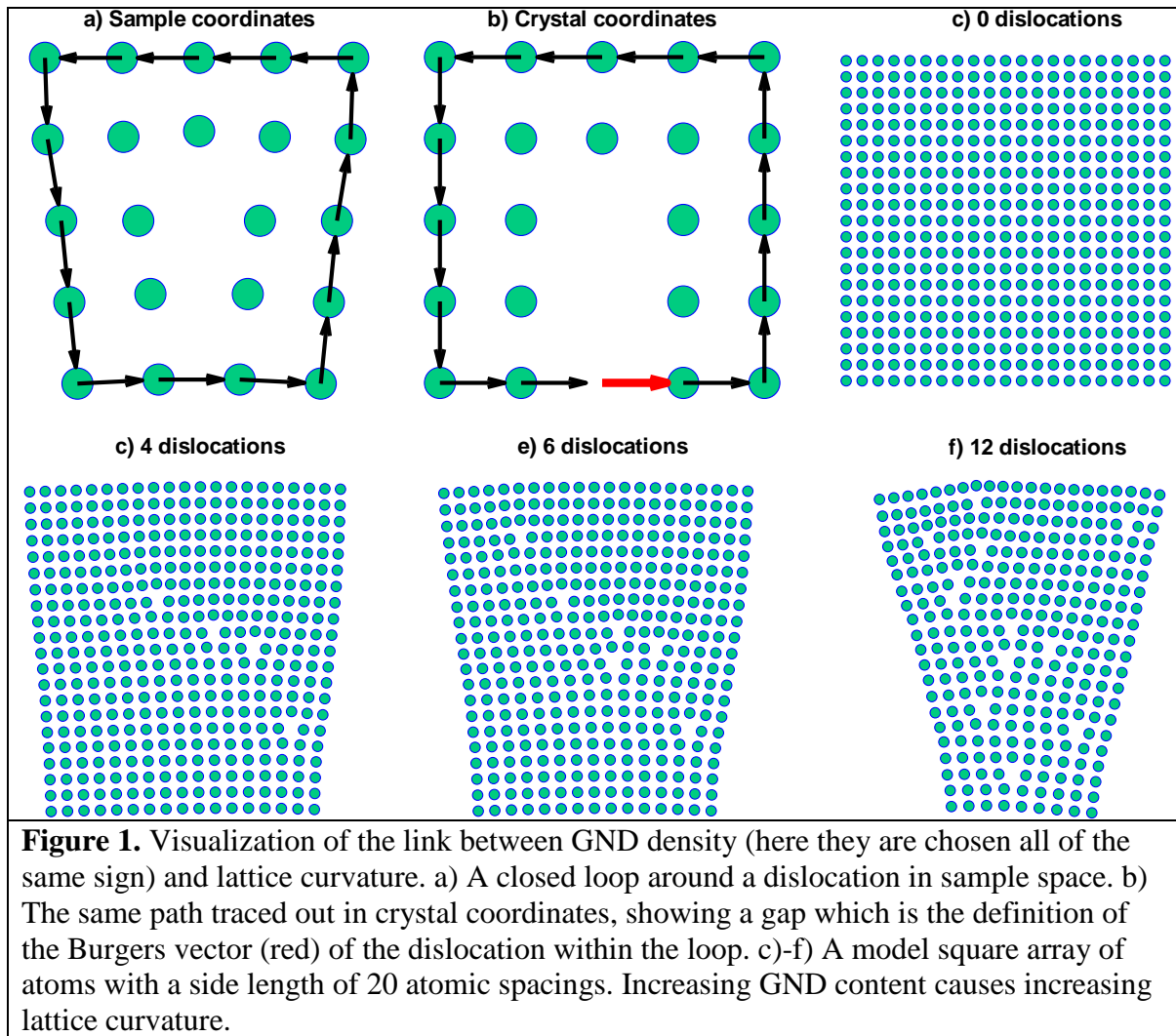
In this contribution we summarise a method for extracting information on GNDs from EBSD data which is fast and is based on just a few simple assumptions. It has been used in several studies (Table 1) since it was devised (Wheeler et al., 2009), and we show how it is used in practice. We explain the method using model distorted crystals, with mathematical details in Supplementary Information. We discuss how the method applies to smoothly curved lattices and to subgrain walls (where GNDs are collected into surfaces of negligible width). We present a new analysis of the errors inherent in the calculation, so that hypotheses about microstructural evolution can be tested robustly. We present new examples of the method in use on olivine and plagioclase and discuss previous studies in the light of our error analysis. Finally, we discuss this method in relation to others used to analyse intracrystalline distortion and suggest future developments. We note that the methods discussed here are applicable to any crystalline material including metals, ceramics and ice.

## 2. The WBV technique

The technique gives information on combinations of GND Burgers vectors and GND densities, so we now discuss these two concepts. The Burgers vector of a dislocation can be thought of as the unit cell mismatch we find if we walk round a dislocation and come back to our start point (Fig. 1a, b)). It can be described in crystal coordinates (hence dimensionless, for example  $[100]$ ) or in sample coordinates (dimensions of length; direction depends on sample orientation). Dislocation density is a phrase which is used in different ways. It may refer to the total line length of Statistically Stored Dislocations in a unit volume. Not all of these give rise to lattice curvature so here we consider the total line length of GNDs per unit volume. We illustrate the basic ideas using a 2D model first.

### 2.1. Concepts in 2D

GND density relates to lattice curvature and a 2D description illustrates this most simply. We show here how curvature relates to single then multiple dislocation populations. Figure 1c)-f) shows lattice orientations in a 2D model which can, at each point, be described by a single number (angle  $\theta$  of a particular lattice direction anticlockwise from a reference direction). In 2D all dislocations have edge character and in the figure the Burgers vectors are defined as one atomic spacing so  $\mathbf{b} = [10]$ . The four frames show increasing dislocation density  $\rho$ , defined in 2D as the number of dislocations per unit area, and the corresponding increase in lattice curvature. The irregular spacing of dislocations means this model is an approximate illustration but provides a basis for understanding.



EBSD measurements do not pick out individual atoms but provide orientation  $\theta$  as a defined function of position (in 2D,  $\theta(x, y)$ ); that is what we must work with. Lattice curvature is defined by variations in  $\theta$  in the  $x$  and/or  $y$  directions. The lattice curvature is then a vector

$$\boldsymbol{\kappa} = -\left(\frac{\partial\theta}{\partial x}, \frac{\partial\theta}{\partial y}\right) \quad (1)$$

(see Appendix 2.1 for details) and relates to a single population of GNDs by

$$\boldsymbol{\kappa} = \rho \mathbf{b}$$

which incorporates the fact that in sample coordinates,  $\mathbf{b}$  may vary even if it is a single crystallographic direction. Considering just the magnitudes, we can write this as

$$(\text{curvature}) = (\text{dislocation density}) \times (\text{Burgers vector length})$$

which is a starting point for understanding the link between curvature and dislocation density. If there is more than one type of dislocation (each with different Burgers vectors and densities)

$$\boldsymbol{\kappa} = \sum_N \rho^{(N)} \mathbf{b}^{(N)} \quad (2)$$

where  $\rho$  and  $\mathbf{b}$  are the density and Burgers vectors *for each type* (superscript N) of dislocation. If there were just 2 types of dislocation, this equation would yield their densities uniquely. If more than 2 types are present then the densities are non-unique, but the equation still provides constraints. Such issues are relevant for 3D which we now discuss.

## 2.2. Concepts in 3D

In 3D we require three numbers to define a lattice orientation (e.g. conventionally three Euler angles, although other representations are available), and we have three directions in which to evaluate gradients, there are 9 gradients to consider. Nye (1953) showed how curvature is then a second rank tensor, but a more direct link to dislocation density (line length per unit volume in 3D) is established via a tensor  $\alpha$  (which now carries his name), also a function of orientation gradients. This links to dislocation density as follows.

$$\alpha_{i\gamma} = \sum_N \rho^{(N)} b_i^{(N)} l_\gamma^{(N)} \quad (3)$$

where  $\rho$ ,  $\mathbf{b}$  and  $\mathbf{l}$  are the density, Burgers vector and unit line vector for each type (labelled N) of dislocation. Note the close resemblance to eqn 2, but with the extension to include dislocation line vectors. When there are many types of dislocation, there may be multiple combinations giving a particular Nye tensor. Note the following.

- This has to be written in terms of vectors and tensors, since the situation is 3D.
- Such equations are best written using index notation which makes explicit whether vectors are expressed in crystal coordinates (Latin subscript for  $b_i$ ) or sample coordinates (Greek subscript for  $l_\gamma$ ).
- $\alpha$  is sometimes called “dislocation density” but must be distinguished from other uses of the same phrase.

Determining the full Nye tensor requires orientation gradients in all three directions. Although there are GND studies using 3D EBSD from serial FIB milling e.g. (Kalácska et al., 2020; Konijnenberg et al., 2015) these are challenging and generally EBSD is conducted on 2D sections. Wheeler et al. (2009) showed that relevant (though incomplete) information could still be extracted from a 2D map. Specifically, of the 9 components of the Nye tensor, a 3-component vector can be calculated. The vector is a sum of Burgers vectors of GNDs, *weighted* by the actual dislocation density of each type of GND and by the angle between the dislocation lines and the map. Lines at a high angle to the map are favoured and so the phrase “Weighted Burgers Vector” (WBV) was used, to make clear that this vector is a weighted “sample” of the Nye tensor.

$$W_i = \alpha_{i3} = \sum_N \rho^{(N)} b_i^{(N)} l_3^{(N)} = \sum_N \left[ \rho^{(N)} l_3^{(N)} \right] b_i^{(N)} \quad (4)$$

where  $W$  is the WBV, and the subscript “3” refers to the z direction, perpendicular to the map, so  $l_3$  is the component of a dislocation line vector perpendicular to the map: it varies from 0 (lines parallel to map) to 1 (lines perpendicular to map). The terms in square brackets are scalars, so note that the WBV is a linear combination of Burgers vectors – this is one reason why it is a useful quantity. The WBV has units of  $(\text{length})^{-1}$  and it is convenient to use units of  $(\mu\text{m})^{-1}$ . We denote its magnitude as  $W$ . It can be expressed in crystal coordinates as in eqn (4), or in sample coordinates by calculating  $\mathbf{hW}$  where  $\mathbf{h}$  is the orientation tensor (a

function of Euler angles). It might appear that this will give a non-unique answer for the vector in sample coordinates, since  $\mathbf{W}$  has symmetric variants in crystal coordinates, but Appendix 1 shows this is not the case – there is a unique WBV in sample coordinates.

There are two approaches to calculating  $\mathbf{W}$ , differential and integral. The differential method involves evaluating local gradients in  $\mathbf{h}$  around the point at which  $\mathbf{W}$  is required. Since that point has a specific orientation,  $\mathbf{W}$  can be expressed in crystal or sample coordinates. The integral method involves integrating round a closed loop on the map to obtain the *net* or *average* Burgers vector content of the GND lines intersecting the map inside the loop, expressed in crystal coordinates. The mathematics in essence defines the loop in sample coordinates (c.f. Fig. 1a) black arrows), transforms each loop segment (black arrow) into crystal coordinates (c.f. Fig. 1b) black arrows), and sums up the segments in crystal coordinates to give the net Burgers vector (red arrow). Unlike the differential method, there is no strict way to express the vector in sample coordinates because orientation varies around and within the loop and the result of the integral method is not linked to any particular point within the loop. However, as we discuss below, for the calculation to be meaningful there should be no large orientation variations around the loop. In that case the orientation at, for example, the loop centroid could be used to convert from crystal to sample coordinates.

If the orientation  $\mathbf{h}$  is a defined mathematical function of position, then the methods are identical (they are related by Stokes' theorem). In practice  $\mathbf{h}$  is defined at discrete measurement points, e.g. on a square grid. The differential method then involves numerical estimation of orientation gradients, with some flexibility in terms of the number of points used. The integral method involves numerical integration around the closed loop. As we will show later, the methods have different advantages in practice.

### 2.2.1. WBV, lattice vectors and Burgers vectors

In this section we discuss the links between WBV and Burgers vectors and show how there may be unique or non-unique relationships. In the approach we describe here, the “differential” values of WBV are usually expressed in units of  $(\mu\text{m})^{-1}$ . In crystal coordinates  $\mathbf{W}$  can be decomposed into lattice basis vectors  $\mathbf{L}$  if needed

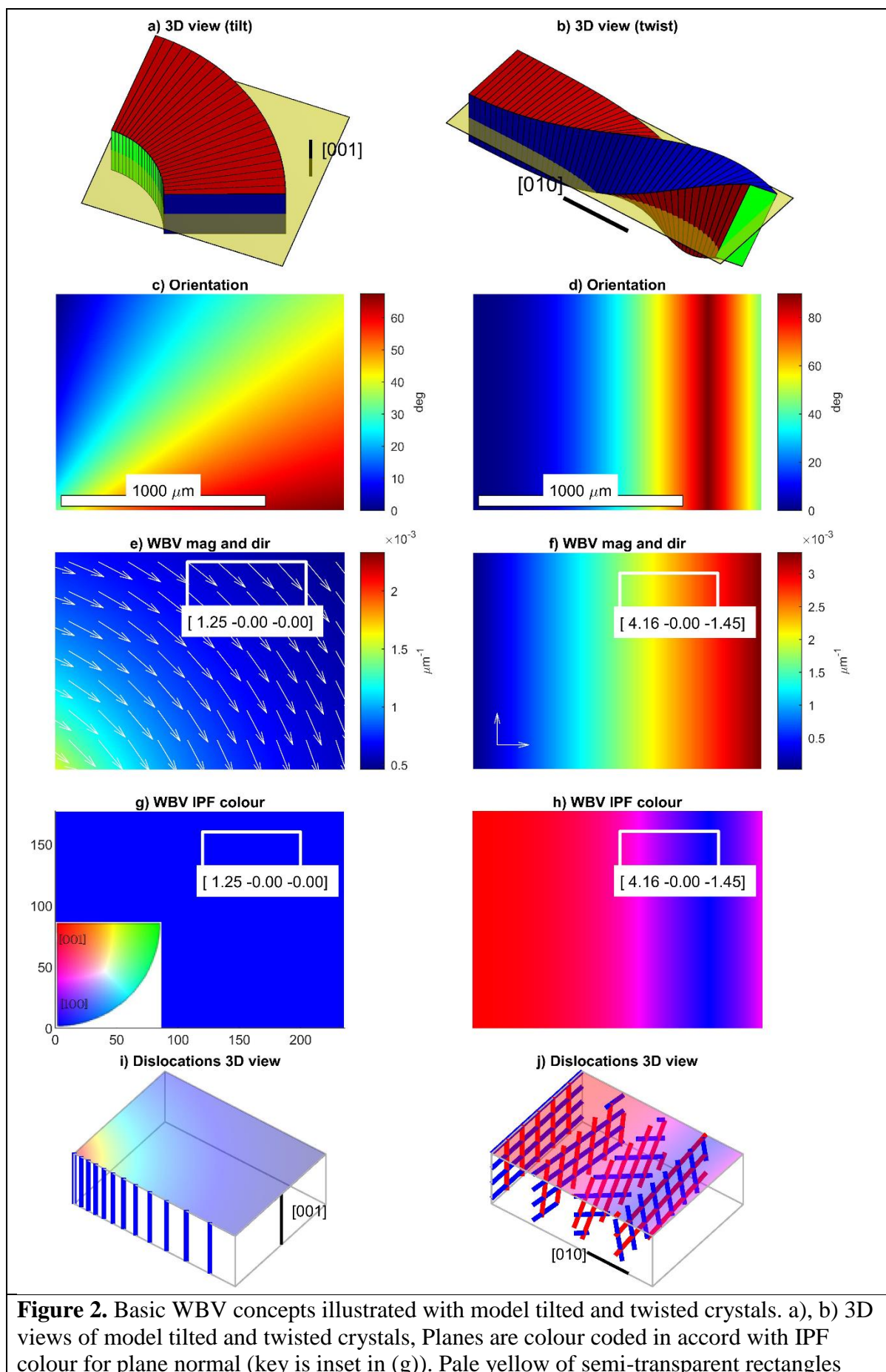
$$\mathbf{W} = K_1\mathbf{L}_1 + K_2\mathbf{L}_2 + K_3\mathbf{L}_3 \quad (5)$$

where the coefficients  $K$  are in units of  $(\text{length})^{-2}$ . These coefficients *resemble* dislocation densities but are in general different. This decomposition relates to the GND types and densities and is unique but further assumptions are needed to express it in terms of the Burgers vectors of actual slip systems. For example, in olivine, if we find that  $\mathbf{W}$  is parallel to [203] and we know the distortion is due to crystal plasticity then we can deduce that it shows a combination of slip systems with [100] and [001] Burgers vectors. The magnitude of  $\mathbf{W}$  parallel to [100] would then, in accord with eqn (4), be a weighted sum of the dislocation densities of all types of dislocation with [100] Burgers vectors. In anhydrite, also orthorhombic, slip systems can involve [001], [1-1-2] and [11-2] Burgers vectors (Hildyard et al., 2009). There is a unique way to express the three components of  $\mathbf{W}$  in terms of those three vectors, if those vectors are linearly independent: in this example  $[203] = 7[001] + [1-1-2] + [11-2]$ . However, many crystals have more than three Burgers vectors for possible slip systems, especially in more symmetric crystals counting all symmetric variants. For example, in a trigonal phase such as calcite, there will be at least 3 Burgers vectors in the basal plane.

Any two of these can be combined to give the basal plane component of  $\mathbf{W}$ , so the decomposition is non-unique.  $\mathbf{W}$  still carries valuable information on the relative contributions of dislocations with basal and non-basal Burgers vectors (Chauve et al., 2017). Our philosophy here is that the methods give the value of  $\mathbf{W}$ , and if further assumptions are required (in terms of expected slip systems, relative energies etc.) these should be made on a case-by-case basis. The  $K$  coefficients can be related to GND densities using further information such as the specific Burgers vectors of GNDs.

It is crucial to note that the WBV cannot generate “phantom” directions: it must be the weighted average of Burgers vectors that are actually present in the microstructure. For example, whether the mineral is olivine or anhydrite or some other phase, if  $\mathbf{W}$  is  $[203]$  then *at least one* of the GND types involved *must* have Burgers vector with an  $[001]$  component, though not necessarily parallel to  $[001]$ .

We next illustrate how to visualise and interpret the WBV, using models for a smoothly tilted lattice, a smoothly twisted lattice (for illustration, distortions are much larger than those found in real crystals) and a tilt subgrain wall. The models have no variation of orientation in the  $z$  direction and the Nye tensors can be calculated fully (Appendix 2).



indicates the map plane. c), d) Misorientation relative to top-left corner for tilt and twist models. In c) misorientation is around the [001] axis which points out of the page. In d) misorientation is around the [010] axis, running left-right, with linearly increasing gradient of twist angle to right. e), f) WBV magnitude (in  $\mu\text{m}^{-1}$ ) colour coded for each model. In e) actual vector directions shown as white arrows; in f) WBV directions point directly into page so are not shown. The boxes are example integration loops with the net WBV indicated as  $K$  coefficients in  $(\mu\text{m})^{-2}$ . g), h) WBV direction colour coded for each model. Inset shows IPF key. i) 3D view of semi-transparent WBV magnitude map for tilt model (as in (e)), with edge dislocations lines shown schematically: parallel to [010] and colour coded in accord with their [100] Burgers vectors. j) 3D views of semi-transparent WBV direction map for twist model (as in (h)), with two sets of screw dislocations lines shown schematically: blue parallel to [100], red parallel to [001]. For visual clarity the dislocations are shown as if in walls, but the distortion gradient is actually smooth. Note how the “weighting” towards dislocation lines perpendicular to the map causes variation in WBV direction (as in f) although the relative density of the two types of dislocation is actually uniform in 3D.

### 2.2.2. Model of smoothly tilted crystal

This model is similar to Fig 1, with a 3D view shown in Fig. 2a). The lattice is misoriented relative to the y-axis by an angle  $\theta$  (zero along the y-axis and  $< 0$  to the right), Fig. 2c). The misorientation axis is [001] which points out of the page. The centre of curvature is beyond the bottom left of the map (Fig. 2c)). If  $r$  is the distance to this centre, it is the radius of curvature of the lattice and in sample coordinates

$$\mathbf{W} = \frac{1}{r}(\cos \theta, \sin \theta, 0)$$

and in crystal coordinates,

$$\mathbf{W} = \frac{1}{r}(1, 0, 0) \quad (6)$$

The magnitude of  $\mathbf{W}$  is shown in Fig. 2e), increasing towards the centre of curvature in accord with eqn. (6). The WBV is a vector which can be represented in sample or crystal space: these require different methods for visualising direction. In sample space WBVs can be displayed as arrows on a map as in Fig. 2e). The direction in crystal coordinates is colour coded (as in any other sort of IPF map) in Fig. 2g), with the IPF colour scheme inset. Since  $\mathbf{W}$  is everywhere parallel to [100] we see a single colour. The rectangle is an integral loop labelled with its net Burgers vector content in units of  $(\mu\text{m})^{-2}$ ; note only the first [100] component is non-zero.

Multiple decompositions of  $\mathbf{W}$  are possible, but the simplest is a single population of edge dislocations with lines parallel to [001], Burgers vectors parallel to [100] and density

$$\frac{1}{ar}$$

where  $a$  is the length of [100]. Fig. 2i) shows a 3D view of that model. If this were not a model, all the map and WBV data could be in accord with other interpretations, for example dislocation lines not parallel to  $z$ . However, *any* interpretation must involve dislocations with

Burgers vectors with a [100] component: the WBV calculation cannot generate “phantom” components (see above).

### 2.2.3. Model of smoothly twisted crystal

This model illustrates the importance of understanding the “weighting” or stereological bias in the WBV calculation. In Fig. 2b) the twist is defined by misorientation by angle  $\theta$  around the [010] axis, with  $\frac{d\theta}{dx}$  increasing to the right. Fig. 2d) shows the misorientation relative to the top-left corner; because this is olivine, symmetry dictates that the misorientation reaches a maximum at 90 degrees then decreases rightwards even though the lattice is more twisted to the right and the angle  $\theta$  used for calculations increases monotonically. In sample coordinates (appendix 2.2) we have

$$\mathbf{W} = \frac{d\theta}{dx}(0, 0, -1)$$

In crystal coordinates

$$\mathbf{W} = \frac{d\theta}{dx}(\sin \theta, 0, -\cos \theta) . \quad (7)$$

The magnitude of  $\mathbf{W}$  is simply  $\frac{d\theta}{dx}$  and increases linearly to the right because  $\theta$  is quadratic in  $x$  (Fig. 2f)). WBV arrows in sample coordinates are not shown for the twist example because they all point vertically out of the map. In crystal coordinates the direction of  $\mathbf{W}$  varies sinusoidally with  $\theta$  (Fig. 2h)). The rectangle is an integral loop labelled with its net Burgers vector content in units of  $(\mu\text{m})^{-2}$ ; note both [100] and [001] components are non-zero, in agreement with the presence of blues and purples within the loop. The variation in WBV direction across the map could be interpreted to mean that different types of dislocation predominate in different parts of the model. This is not the case: it is a stereological effect and needs careful explanation now because such effects must be borne in mind in any study.

Multiple decompositions of  $\mathbf{W}$  are possible, but the simplest is as a sum of contributions from screw dislocations parallel to [100] with a density of

$$\frac{1}{a} \frac{d\theta}{dx}$$

and screw dislocations parallel to [001] with a density of

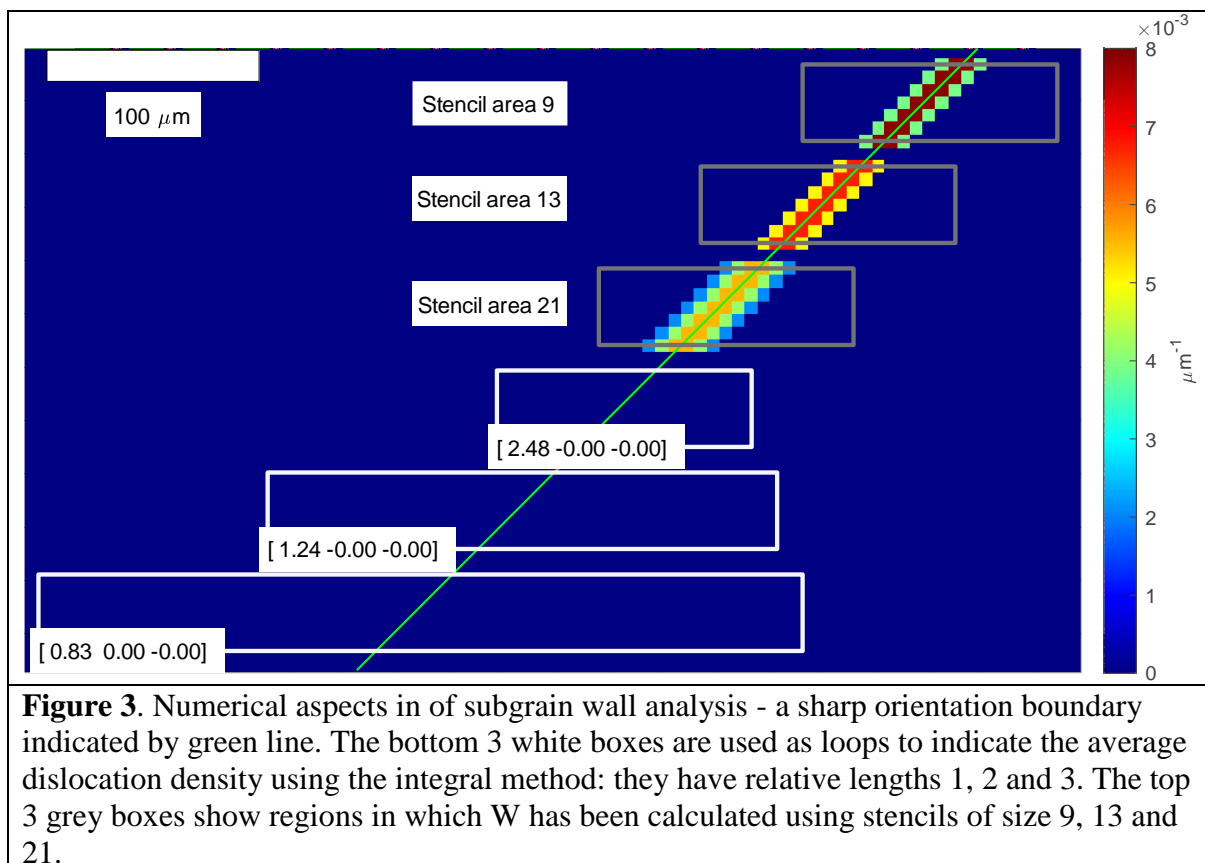
$$\frac{1}{c} \frac{d\theta}{dx}.$$

This decomposition is show in Fig. 2j). The dislocation lines are coloured using the IPF colour scheme for *line direction* (as in Fig. 2g)) but since these are screw dislocations the colours also indicate Burgers vector directions. Consider the model near the left hand end where  $\theta$  is small. Blue [100] dislocations are almost parallel to the map. This means the WBV calculation does not “sample” them and the IPF colour (Fig. 2h)) is dominated by red [001]. As the lattice is more twisted passing to the right, [100] lines are at higher and higher angles to the map. Hence the WBV IPF map is more dominated by blue. At a position near the right hand side of the map, [001] lines are parallel to the maps so are not sampled at all; the IPF map is blue. As  $\theta$  increases beyond 90 degrees we see an influence of [001] reappear. This is an example of the “weighting” towards dislocation lines at a high angle to the map.

The twist structure illuminates some fundamental aspects of WBV. The displays are entirely in accord with eqn. (7) and the WBV provides a weighted “subset” of the full dislocation population. If we were to examine another map at right angles to the one considered (but still containing the twist rotation axis) this second map would show a preponderance of [100] vectors at the left end, with more [001] passing to the right – it would look quite different.

#### 2.2.4. Model of subgrain tilt wall

Many microstructures contain subgrain walls which, although populated by GNDs, have in essence zero width and hence zero volume. This means that dislocation density, defined as line length per unit volume, is infinite. Similarly, a sharp change in orientation means the lattice curvature is infinite. So, although eqn. (4) still applies, it is not particularly helpful. In contrast the integral method still yields finite values when the loop crosses a subgrain wall. Now, though, the quantities obtained are highly dependent on the size of the loop chosen for integration: the area does not affect the net Burgers vector content  $\mathbf{B}$ , only the length of subgrain wall intersected by the loop. The software we have developed delivers a vector  $\mathbf{B}/A$  with units of  $(\text{length})^{-1}$  to characterise the GND content of a loop. Fig. 3 (lower part) shows three loops, each intersecting the same length of subgrain wall and having the same value of  $\mathbf{B}$ . However, the areas differ and so the values of  $\mathbf{B}/A$  differ.



The numbers from WBV calculations are meaningful where the areas being analysed have orientation variations due to GNDs. High angle boundaries must therefore be excluded from consideration since they do not have a dislocation substructure. There is no single “cutoff” angle applicable to all phases; in the algorithms we have created, the user chooses the angle and then high angle boundaries are excluded from calculations, as we describe below.

To this point no discussion has been required about the finite number of measurement points that comprise an EBSD map, and the consequences for gradient calculation. Our models are based on algebraic descriptions of distorted lattices (see Appendix 2). Now we need to discuss the consequences of two numerical aspects of EBSD measurements: that they are made at discrete points, and that they have errors in orientation.

### 2.3. Numerical aspects of analysing spaced EBSD measurement points

Orientation data to be analysed are not mathematical functions of position but discrete measurements at scattered measurement points (hereafter, simply “points” for brevity). The calculation methods therefore involve numerical approximations to the gradients and integrals of the underlying theory, and the differential and integral methods have different advantages in practice. The points in the studies we describe are on square grids, but there is no reason why the method should not be extended to hexagonal or other grids.

#### 2.3.1. Differential method

The differential method uses gradients in orientation in  $x$  and  $y$  to calculate the WBV. A numerical estimation of gradients uses 2 or more orientation measurements and the distances between the points. We call the cluster of points used a “stencil” (Fig. 4a)). For flexibility our software allows for different stencil sizes; the differential method calculates a “best fit” lattice curvature using the orientations at each point in the stencil. Using larger stencils reduces errors in calculation (discussed later), but at the same time “smears out” microstructural details on the scale of the stencil. In published works the  $P = 9$  stencil has usually been used; we discuss the effects of stencil size in the section on accuracy below.

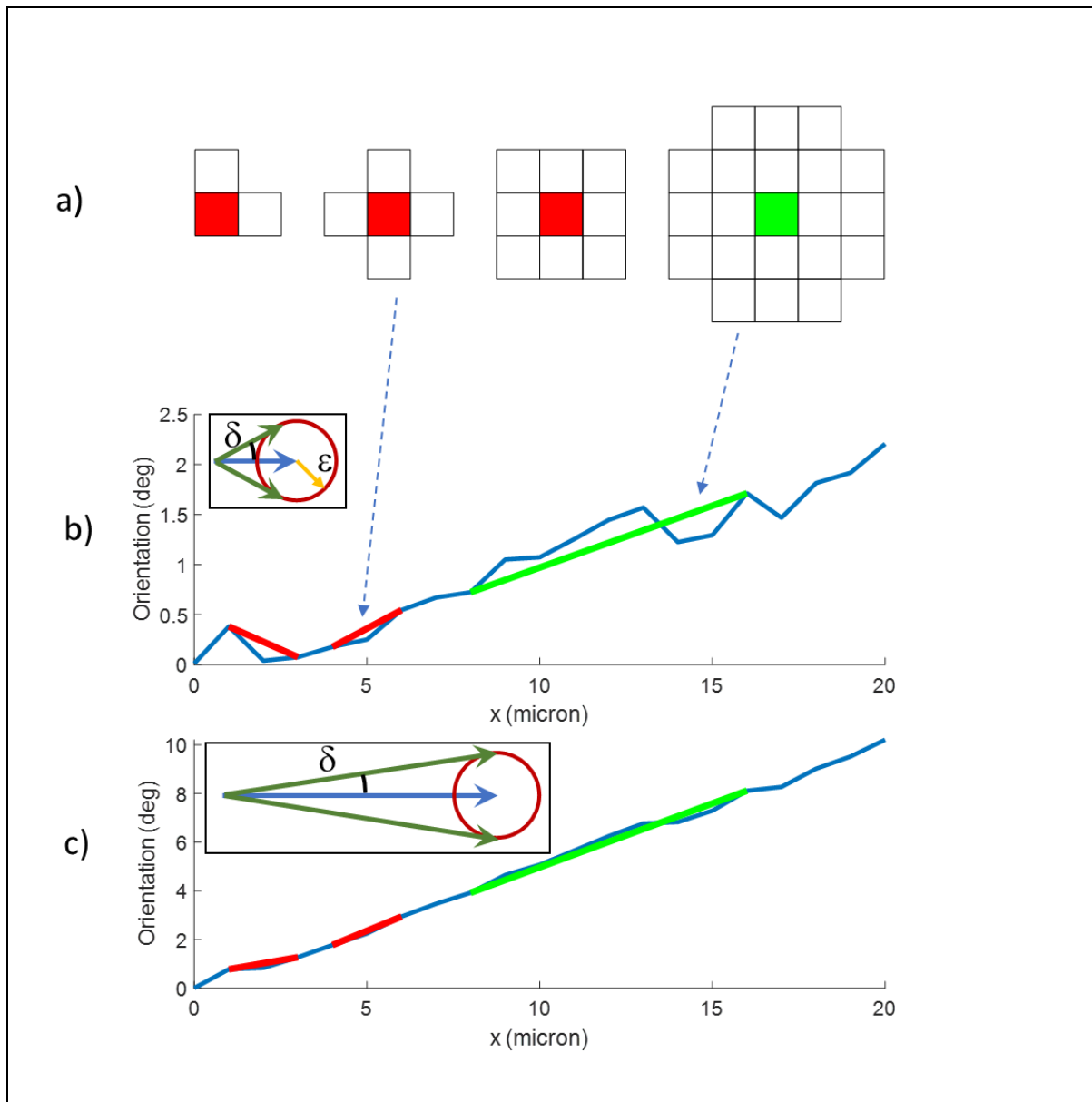


**Figure 4.** Stencils and errors in WBV. a) “Stencils” are arrangements of nearby points used for numerical calculation of orientation gradients at particular point (coloured). Shown are example stencils of area 3, 5, 9 and 21. b) Simple illustration of effects of orientation errors. Blue graph shows a low but uniform orientation gradient (in 1D) with errors imposed. Red lines show the large effects of errors on estimating gradients over a short segment (analogous to using a small stencil). Note the estimate may even have the wrong sign. Green line shows the improved precision using a longer segment (analogous to using a larger stencil as in a)). Inset illustrates consequent angular error in WBV direction (in 2D). The actual WBV is shown as blue arrow but with error  $\epsilon$  (related to the gradient error) so WBV values might fall in orange circle. Green arrows illustrate the range of directions and hence the angular error  $\delta$  that would arise due to these errors. c) As in b), with the same errors imposed, but for a larger orientation gradient. The errors in slope are the same as in b) but are *proportionately* less. The error  $\epsilon$  in WBV is the same as in b) and the size of the error circle is the same for both. However, the angular error  $\delta$  is smaller in c) because the WBV is longer.

In a previous section we pointed out that if a subgrain wall is considered as having zero width, it will have infinite dislocation density. Because of this numerical differentiation creates numerical artefacts as it uses spaced measurement points. The algorithm cannot distinguish a sharp orientation change between two points from a smooth orientation gradient between those points. A consequence is that if a subgrain wall is present, the apparent WBV magnitude will be finite and depend on step size, so should be interpreted with care. In practice we find that narrow “swathes” of high  $W$  are common on calculated  $W$  maps and are likely to be subgrain walls. In this case the magnitude  $W$  must be interpreted with care but the WBV direction still contains information on the Burgers vectors of the GNDs in the subgrain wall. The top 3 boxes in Fig. 3 indicate the calculated  $W$  values for a sharp orientation boundary, using the differential method with stencils with areas 9, 13 and 21. Note how the dislocation density is smeared out more for larger stencils, and has apparently lower values.

### 2.3.2. Integral method

The integral method involves integrating the orientation tensor around a closed loop in the map plane, directly giving the net Burgers vector sum for all the dislocation lines threading through that loop. To undertake this numerically, our studies to date have restricted loop shapes to rectangles, though there is no fundamental difficulty in implementing other shapes. The result of integration is a vector  $\mathbf{B}$  with dimensions of length. We divide this by the loop area  $A$  to get a vector in  $(\text{length})^{-1}$  which is more easily compared to results of the differential method. Algebraically, the vector  $\mathbf{B}/A$  must equal the average  $\mathbf{W}$  value in the loop (eqn. (6)). Numerically, the “best fit” algorithm used in the differential method means the methods may give slightly different results.

The integral method was first developed as an exploratory tool in which the user drew rectangular loops and the WBV was reported as a lattice vector (e.g. Fig 2e, f)). We have recently developed a method of systematically “tiling” the map with square loops, and applying the integral method to each loop as in Fig. 8c of Timms et al. (2019). In all circumstances, if the loop crosses a high angle boundary then a WBV can in principle be calculated but, as discussed above, has no meaning - so instead the algorithms we use do not return a result. The tiles can be displayed colour coded by standard IPF colour schemes using a  $W$  threshold, in the same way as for calculations made with stencils (examples are given later). The tiles can be thought of as large pixels, though not all properties are precisely analogous to those of individual measurement points.

### 2.4. Numerical aspects of dealing with orientation measurement errors

Orientation measurements used may be in error as a result of errors in the Hough transform, up to a degree at most (Prior et al., 2009); for one study on an Si single crystal, was  $0.2^\circ$  (Ram et al., 2015). Improved “real time” approaches to indexing Kikuchi patterns reduce the angular error in orientations to  $<0.05^\circ$  (Nicolay et al., 2019). For higher angular resolution methods, e.g. correlating Kikuchi patterns, errors may be as low as  $\sim 0.0003$  radians (Wallis et al., 2019a). The differential method uses gradients in crystal orientation to calculate WBV. On the grid of measurement points, a gradient is calculated from the misorientations between adjacent measurements. The misorientation angles are likely to be small and so the errors in misorientation axes will be large (Prior, 1999) and these errors will propagate into the WBV calculation. An algebraic analysis would involve error propagation through operations on various orientation tensors and is beyond the scope of this contribution; instead, we use simple arguments followed by some numerical experiments.

### 2.4.1. General nature of error effects

We argue in this section that angular errors in WBV are smaller for long WBVs. Longer WBVs are linked to higher lattice curvatures. Higher lattice curvatures mean the misorientation angles between adjacent pixels are larger, and the misorientation axes will have smaller errors, and the WBV direction will have smaller errors. We illustrate this assuming a typical orientation error of 0.01 radians.

Benchmark curvature (above which calculation will be less error prone)  $\sim 0.01/(\text{step size})$   
and in terms of magnitude

$$|\text{WBV}| \sim \text{curvature}$$

which means we should consider a benchmark below which WBV is error-prone as

$$|\text{WBV}| \sim 0.01/(\text{step size}) = W_t$$

This approach is similar to the derivation of eqn. 13 of Wilkinson and Randman (2010) and eqn 2 of Jiang et al. (2013), where a lower limit on detectable dislocation density is given in terms of step size:

(Minimum detectable GND density)  $\sim$

$$(\text{Angular resolution}) / ((\text{step size}) * (\text{Burgers vector length}))$$

For example  $0.01 / ((1 \text{ micron}) * (5 \text{ angstrom})) = 2 \times 10^{13} \text{ m}^{-2}$

The approach described below is related because in order of magnitude,  $W = \rho b$ . Hence our  $W_t/b$  equates to the minimum detectable GND density discussed in other work. That work, and others (by the group) focusses on accuracy in determining dislocation *density*; here we also analyse WBV *direction* since it plays a key role in several studies (Table 1). In Wheeler et al. (2009) we argued that longer WBVs would be more accurate in terms of direction. For example, the map of Mg used in Fig. 2 and 3 of Wheeler et al. (2009), modified in Fig. 5, has a step size of  $4 \mu\text{m}$  so  $W_t = 0.0025 \mu\text{m}^{-1}$ . Fig. 5 shows considerable scatter for  $W > 0.002 \mu\text{m}^{-1}$  and much less for  $W > 0.004 \mu\text{m}^{-1}$ , in accordance with the argument that  $W_t$  offers a guide to judging precision. Guided by this, our approach to displaying WBV data involves selecting data based on ranges of  $W$ . The minimum value  $W_{\min}$  in the range will be associated with the maximum angular error. Setting it high will reduce error. The maximum value  $W_{\max}$  is less important but is useful for dividing up datasets.

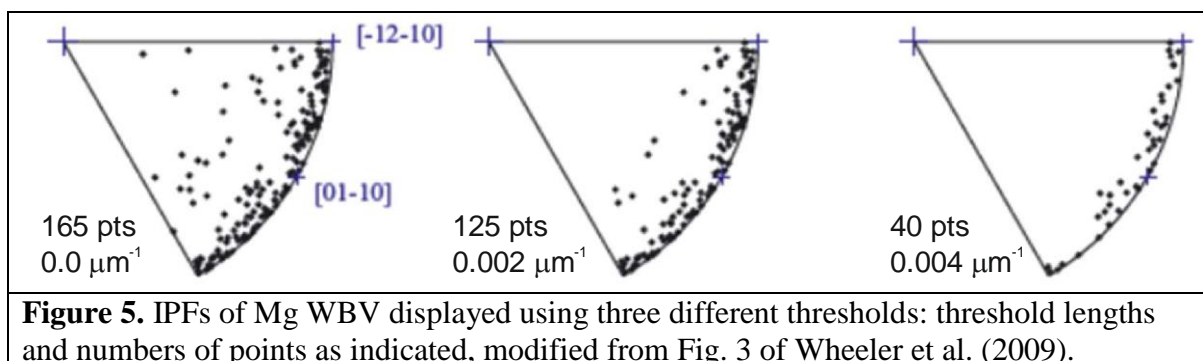


Figure 4b) and c) are non-rigorous illustrations of error effects. The graphs illustrate that larger stencils will give better precision. Errors  $\varepsilon$  in gradients are independent of the gradients themselves but for larger orientation gradients (as in Fig. 4c)), longer WBVs) the errors are *proportionately* less important. The insets in b) and c) illustrate the consequent effects on angular errors. The errors in WBV are now drawn as circles around the actual values since errors may be in any direction. The error circles are the same size in b) and c). The green arrows mark the vectors with maximum angular error  $\delta$ , showing that longer WBVs in c) will have smaller angular errors. In the next section we analyse error effects using numerical models.

#### 2.4.2. Specific analyses of error effects

It is useful to quantify error estimates for WBV, incorporating the effects of WBV length and other parameters. We define an angle  $\alpha_{95}$  so that there is a 95% chance that the true WBV direction is that angle or less from the calculated direction, an approach used in analysing palaeomagnetic data for example Butler (1992). In essence  $\alpha_{95}$  defines a cone of directions within which the true direction is likely to be. This is analogous to the  $\pm 2$  standard deviation range within which 95% of the data lie when dealing with a one-dimensional normal distribution. Our approach gives the angular error for the WBV in sample coordinates: it is in principal the same for crystal coordinates except crystal symmetry may modify the interpretation, as addressed in Appendix 3.1.

EBSD orientation errors will depend on mineralogy, acquisition conditions and indexing methods and will propagate in the WBV calculations. For illustration we create model orientation maps with angular errors in orientation up to  $0.57^\circ$  (0.01 rad) – so our angular error estimates for WBVs are likely to be pessimistic. We used theoretical models shown in Fig. 2 with added orientation noise, and calculated  $\mathbf{W}$  for the noisy datasets. Larger stencils and tiles take into account more orientation measurements and, in common with other averaging techniques, we hypothesised in Wheeler et al. (2009) that this would give higher precision. We examine this idea in Appendix 3. First, we calculate the error on WBV, by comparing actual  $\mathbf{W}$  and theoretical  $\mathbf{W}_c$  values. We find that the error in WBV magnitudes  $\mathbf{E} = \mathbf{W} - \mathbf{W}_c$  are not strongly dependent on length  $W$ , or on whether the model is tilt or twist, but they do depend on stencil size. To quantify the errors, we calculate a standard deviation  $\sigma$  for the vector  $\mathbf{E}$  as described in Appendix 3. Larger stencils and tiles give smaller errors (Fig. 6). So, if one uses stencils (i.e the differential method), there is an approximate relationship between  $W$  precision and the area  $S$  of a stencil (number of points, hence dimensionless)

$$\sigma_S = 0.0247S^{-1}/u \quad (7)$$

where  $u$  is step size.

If one uses tiles (i.e. the integral method) and defines the dimensionless area  $T$  of a tile the standard deviation  $\sigma_T$  of vector  $\mathbf{E}$  is:

$$\sigma_T = 0.0081T^{-3/4}/u . \quad (8)$$

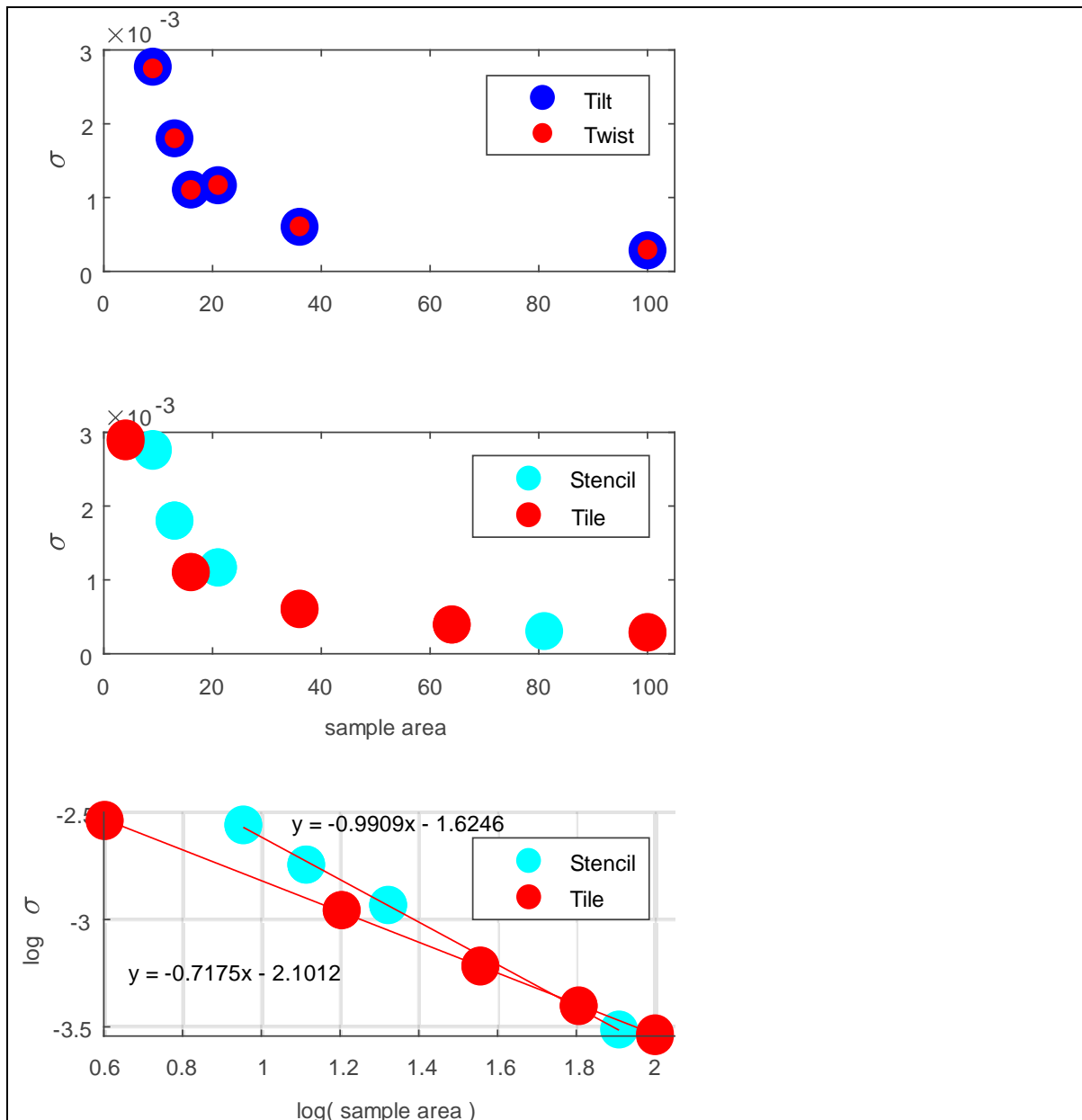


**Figure 6.** a) Standard deviation  $\sigma$  of nondimensionalised WBV magnitude plotted against calculation region size for tilt and twist models, showing errors are independent of the detailed nature of distortion. The three left-hand points are for stencils, the others are for tiles. b) Same, plotted against areas of stencils and tiles for both tilt and twist models. c) Same as b) but plotted as log-log graphs to show linear relationships.

In Wheeler et al. (2009) we suggested that the integral method would have higher precision than the differential method because numerical integration is less sensitive to errors than numerical differentiation. Our assertion was correct because we were using small stencils ( $P = 9$ ) and large integral loops. Fig. 6 b) and c) show that in fact the precision depends mainly on the area of the tile or stencil used. The integral method remains our favoured method for initial exploration since the calculation is much faster than for a stencil of comparable size.

The second stage of error analysis involves the angular errors. These *do* depend on the length  $W$  as described above and in Fig. 6. The inset in Fig 4c) suggests that  $\delta \approx \varepsilon/W$  when errors

are small. This is in accord with Fig. S1. One might then expect some proportionality between measures of vector error  $\sigma$  and angular error  $\alpha_{95}$  in a more rigorous approach, and this is confirmed in Appendix 3. For small errors we have

$$\alpha_{95} \cong 1.413 \frac{\sigma}{W}$$

For example, in Table 1, for the second Mg example we have a step size of 4  $\mu\text{m}$  and calculated the WBV using a stencil area 9 so  $\sigma_s = 0.000686 \mu\text{m}^{-1}$ . For a WBV length 0.004  $\mu\text{m}^{-1}$  we have

$$\alpha_{95} \cong 1.413 \frac{0.000686}{0.004} = 0.24 \text{ rad} = 13.8^\circ$$

(the table calculation is more precise). If we compare the calculated  $\alpha_{95}$  with Fig. 5c), it is plausible that the dislocations are all basal and we see a scatter up to  $14^\circ$  away from the basal plane, broadly in accord with the calculation. The above assessment of precision should be used with caution, since it assumes a particular range of orientation errors in the measured data, and those errors are dependent on acquisition conditions and the mineral being measured. A larger stencil or tile will give a more precise measure of WBV magnitude and direction, but larger regions are also more likely to contain more than one type of dislocation. There is a trade-off between finding a relatively precise WBV direction in a large region that may contain more than one type of GND, versus finding a less precise direction in a smaller region which may relate to a single type of GND.

Our error analysis is numerical rather than algebraic but simple calculations give confidence that, if other parameters are maintained, the WBV angular error will scale linearly with orientation angular error. Thus, if angular errors are distributed uniformly between 0 and 0.001 rad, we expect angular errors in WBV to be 10 times less than those we present here. Such low indexing errors are now routinely possible, albeit with a trade-off on indexing speed (Nicolay et al., 2019). Improved indexing would allow for use of a smaller stencil or tile ensure a particular level of WBV precision. We note that algorithms that assign interpolated orientations to misindexed or non-indexed pixels may have adverse effects on subsequent WBV calculations. For example, if the orientation value of an adjacent pixel is used, this guarantees that there is a zero orientation gradient between those two pixels, which may have a big (and spurious) influence on the WBV calculation. Ideally, analysis is done only on confidently indexed points. We also urge caution using dictionary indexed EBSD maps (De Graef, 2020) for WBV calculations, because the orientations stored in the dictionary of Kikuchi patterns are discrete and orientation gradients therefore will be stepped. This may give a spurious influence on WBV calculations.

### 3. WBV applications in the Earth Sciences: examples

The published works in Table 1 show a variety of approaches for interpreting WBV. The basic algorithms we use do *not* decompose the WBV down into individual Burgers vectors because to do this requires additional assumptions, dependent on the particular mineral and its microstructural evolution. For example, a WBV parallel to [100] may result from a single population of GNDs with Burgers vectors parallel to [100], or a mix of dislocations with [110] and [1-10]. In some phases, prior knowledge of likely Burgers vectors will mean there

is only one choice for decomposition – e.g. if such a WBV is found in olivine. In the following, we present first two new examples of WBV usage and then comment on published examples.

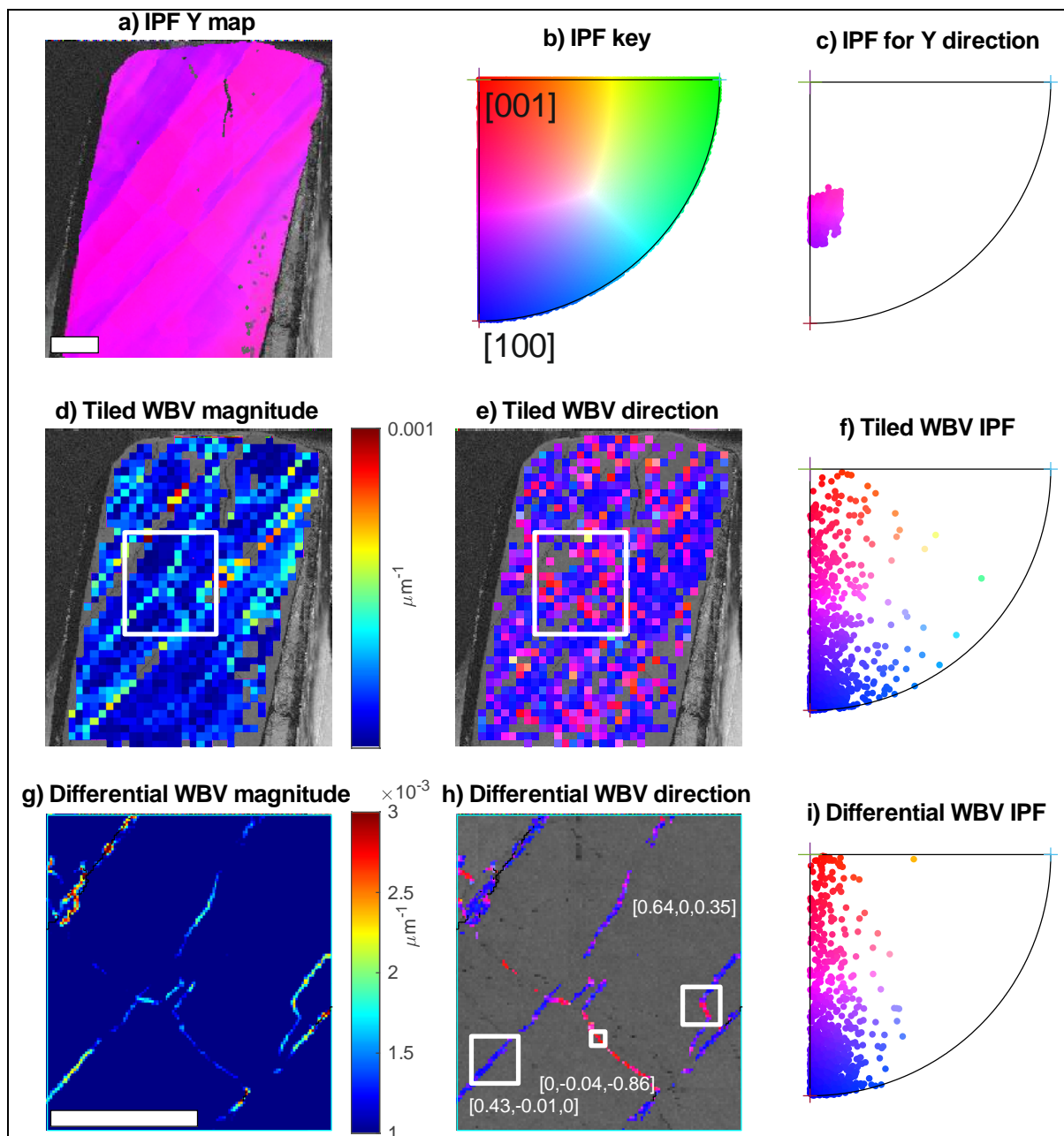


**Figure 7.** Example of WBV applied to olivine. a) IPF map of Y direction of deformed single crystal of olivine. Scale bar is 1000  $\mu\text{m}$ . b) IPF key. c) IPF coloured as in a), showing a few degrees of distortion within a single initially undeformed crystal. d) WBV magnitude map calculated on 10 x 10 tiles. e) IPF map of WBV direction (calculated as in (d)) superimposed on a band contrast greyscale map; minimum length 0.001  $\mu\text{m}^{-1}$ . f) IPF of WBV as in (e). g) WBV magnitude map calculated on 3 x 3 stencils in part of overview map shown as white box in (d). Scale bar is 1000  $\mu\text{m}$ . h) IPF map of WBV direction (calculated as in (g)) superimposed on a band contrast greyscale map; minimum length 0.00005  $\mu\text{m}^{-1}$ , showing subgrain walls with [100] Burgers vectors running NE and those with [001] running NW. White squares indicate results of the integral method, with

numbers in  $\mu\text{m}^{-2}$  expressed as coefficients of crystal basis vectors (K values). i) IPF of WBV as in (h).

### 3.1. Olivine subgrain walls: analysis free from trace, or tilt or twist assumptions

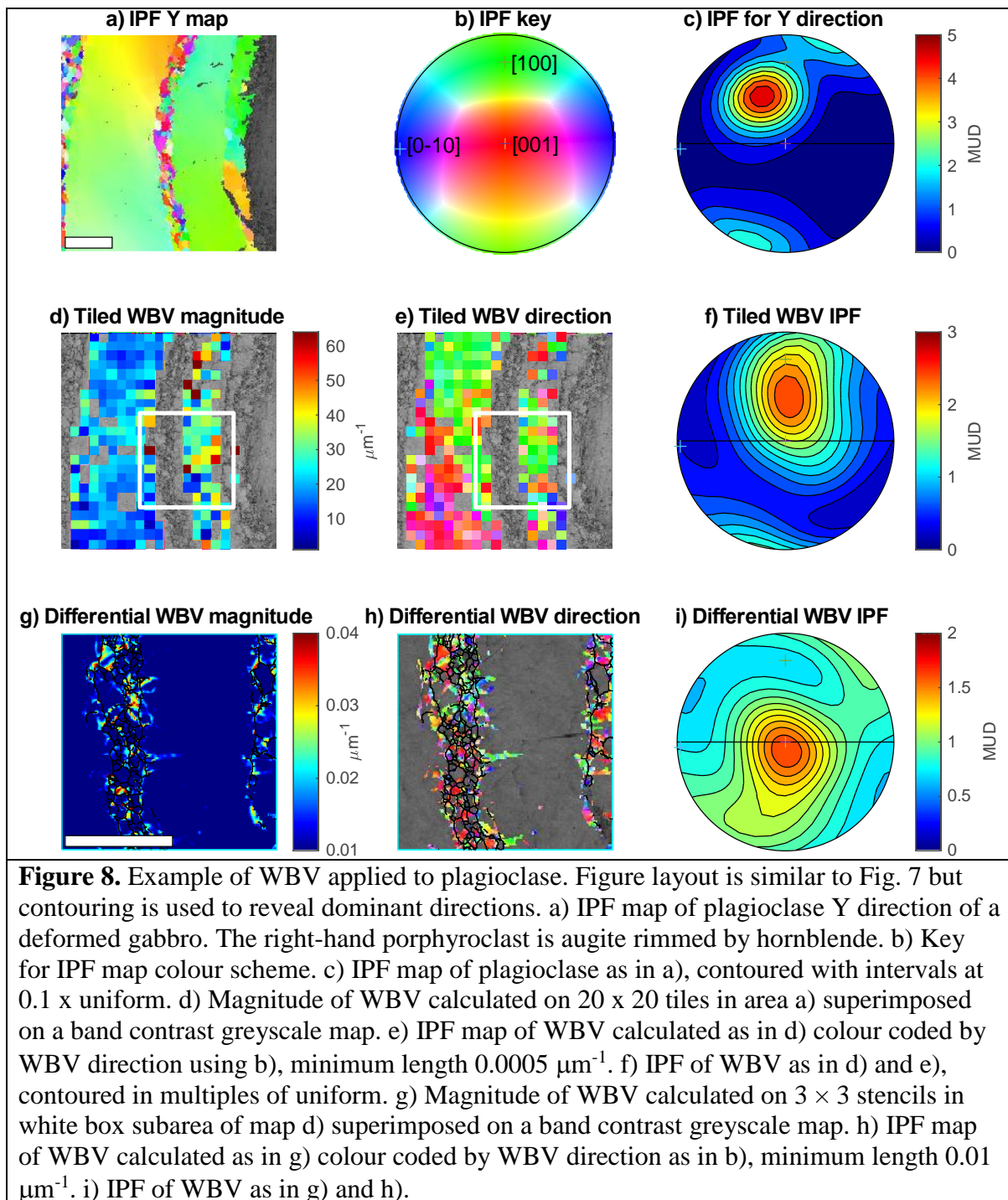
Fig. 7 shows an experimentally deformed single crystal of olivine (PI-1766) as in Fig. 8 of Tielke et al. (2017). The experiment was set up so that the Y (shortening) direction was initially parallel to [101], with an expectation that slip systems with [100] and [001] Burgers vectors. The orientation map (a) shows the crystal direction which is parallel to the Y sample direction, in accord with the IPF key (b). We refer to such maps as “IPF Y maps” below. The colour variations reveal rather straight subgrain walls running in two directions. Orientations vary over a few degrees (c). Fig 7(d) shows 10 x 10 tiles colour coded by WBV magnitude and (e) by direction, superimposed on the band contrast greyscale map. The size of the tiles reduces  $\alpha_{95}$  but the threshold length for display is set low, at  $0.00005/\mu\text{m}$ , so  $\alpha_{95}$  is  $26^\circ$ . With this in mind, the IPF Fig 7f) is, within error, in accord with a mix of dislocations with [100] and [001] Burgers vectors, and the dominant blue colour on the map indicates mainly [100]. Figs (g) and (h) show a subarea with WBV now calculated using a  $3 \times 3$  stencil, giving less precision but more spatial resolution and revealing individual subgrain walls. Blue subgrain walls running NE are consistent with being [100] tilt boundaries and red subgrain walls running SE are consistent with being [001] tilt boundaries. A higher threshold length for display ( $0.001/\mu\text{m}$ ) means  $\alpha_{95}$  is  $14^\circ$  and the IPF in Fig. (i) is in accord with that, insofar as most points are within  $14^\circ$  of the plane containing [100] and [001]. There are still mixtures of [100] and [001]. Some will result from where the stencil overlapped subgrain wall junctions, but as Fig. (h) shows, these mixtures also appear along irregular segments of the NW-SE subgrain walls and are likely to represent two types of GND in an individual wall. The three square “loops” show results of the integral method and provide additional illustration of how the WBV is averaged over the sample area. Each triplet of numbers is a list of K values, i.e. the coefficients defining the WBV when it is expressed in crystal basis vectors (eqn (5)). The numbers have the dimensions of dislocation density but must be interpreted with care, as discussed above and shown in Fig. 3, since the dislocations are in discrete walls.

In this example the directional information is more useful than the density information: integral and differential methods both give information about where GNDs with [100] and [001] occur. Note that examining the subgrain wall traces together with misorientation axes deduced from the distortion (Fig. 7c) could yield similar results. However, that approach would involve manual and subjective selection of boundary segments and of subregions from which to use misorientation data; it would be based on assumptions about pure tilt or twist boundary character and errors would be difficult to assess. Use of WBV does not preclude further analysis (e.g. Wieser et al. (2020)) but provides a firm foundation.

### 3.2. Plagioclase distributed deformation: analysis free from slip system assumptions

Fig. 8 shows plagioclase from a deformed gabbro from close to the slow spreading mid ocean ridge in the SW Indian Ocean (sample ODP 176-735B-95R-2 from approx. 546 m below the ocean floor). The plagioclase is highly strained, with two prominent ribbons bent around an augite porphyroclast (grey scale on right). Trails of smaller grains are interpreted as new grains due to recrystallization. Hornblende marginal to pyroxene suggests deformation is amphibolite facies, as recorded deeper in the leg (Gardner et al., 2020), but it may have been

higher temperature. Our aim here is to not to offer a full interpretation of how the microstructure evolved, but to show how the WBV tools assist in that task.



The IPF Y map (Fig. 8a), colour coded as in 8b) indicates rather smooth variations in orientation for the large grain, in contrast to the olivine example Fig. 7a). Large tiles used in Fig 8d) confirm this, showing a rather uniform level of distortion on the scale of the tiles through the two ribbons. The WBV IPF map (Fig. 8e)) shows  $\langle 100 \rangle$  dominates at the top of the left hand ribbon, whilst  $\langle 001 \rangle$  dominates at the bottom, and the IPF (Fig. 8f)) combines these. In and around new grains no data is displayed (fig. 8d and e) because the  $20 \times 20$  pixel

tiles are large enough to cover several small grains and include high ( $> 5^\circ$ ) angle boundaries. Thus, in these areas WBV analysis is not appropriate. It is worth considering whether the apparent variation in WBV direction is a stereological effect, like that shown in Fig. 2h), j). Could the ribbon have a relatively uniform population of GNDs, but with a stereological bias governed by varying orientation? The misorientation from bottom to top of (for example) the left-hand ribbon is about  $35^\circ$  in contrast to Fig. 2h), j) which involved  $90^\circ$  of twist. We conclude it is likely that there are real variations in the GND population in this grain, which is not surprising given the stretch and non-uniform bending it has enjoyed. Fig 8g)-i) shows WBV calculated using the differential method on a subarea marked with a white box in Figs. 8d and e. In Fig 8g), boundaries above  $5^\circ$  are shown in black and the highest distortions i.e. WBV magnitude are shown not in the large ribbons but in small grains interpreted as products of dynamic recrystallization. Fig. 8h) and i) show WBV direction, with a pronounced maximum close to  $\langle 001 \rangle$  as illustrated by the preponderance of red colours in new grains in (h) and a contoured maximum near  $\langle 001 \rangle$  in (i). The relict ribbon in centre right of Fig. 8h) shows two left-right tapered zones coloured green, indicating WBV rather close to  $\langle -100 \rangle$  and in accord with the tiling in Fig. 8e).

In summary this example shows how the integral (here, tiling) and differential methods may be used to interrogate different parts of the microstructure. The interiors of the plagioclase ribbons have relatively low dislocation densities, with GNDs with Burgers vectors combining  $\langle 100 \rangle$  and  $\langle 001 \rangle$ , likely in different proportions in different parts. Here, the integral method is a very effective tool. For the small grains, interpreted as recrystallized, the differential method is helpful; they have higher dislocation densities and various Burgers vectors but with an emphasis on  $\langle 001 \rangle$ . In tectonites small grains are often interpreted as new, forming by static or dynamic recrystallisation from strongly plastically deformed large old grains, and are relatively strain free. Intriguingly, here the small grains are more distorted than the old ribbons though normally one would expect them to be relatively strain free. Further WBV investigation will assist in understanding the evolution of that microstructure. Methods including the traces of subgrain walls could not be used here, since distortion is distributed; methods assuming slip systems and dislocation line energies could be applied but the required inputs may be difficult to constrain in a mineral like plagioclase. As in the olivine example, we suggest the WBV approach provides a firm foundation on which other analyses can be built if required.

## 3.3. Ice: investigation of non-basal slip

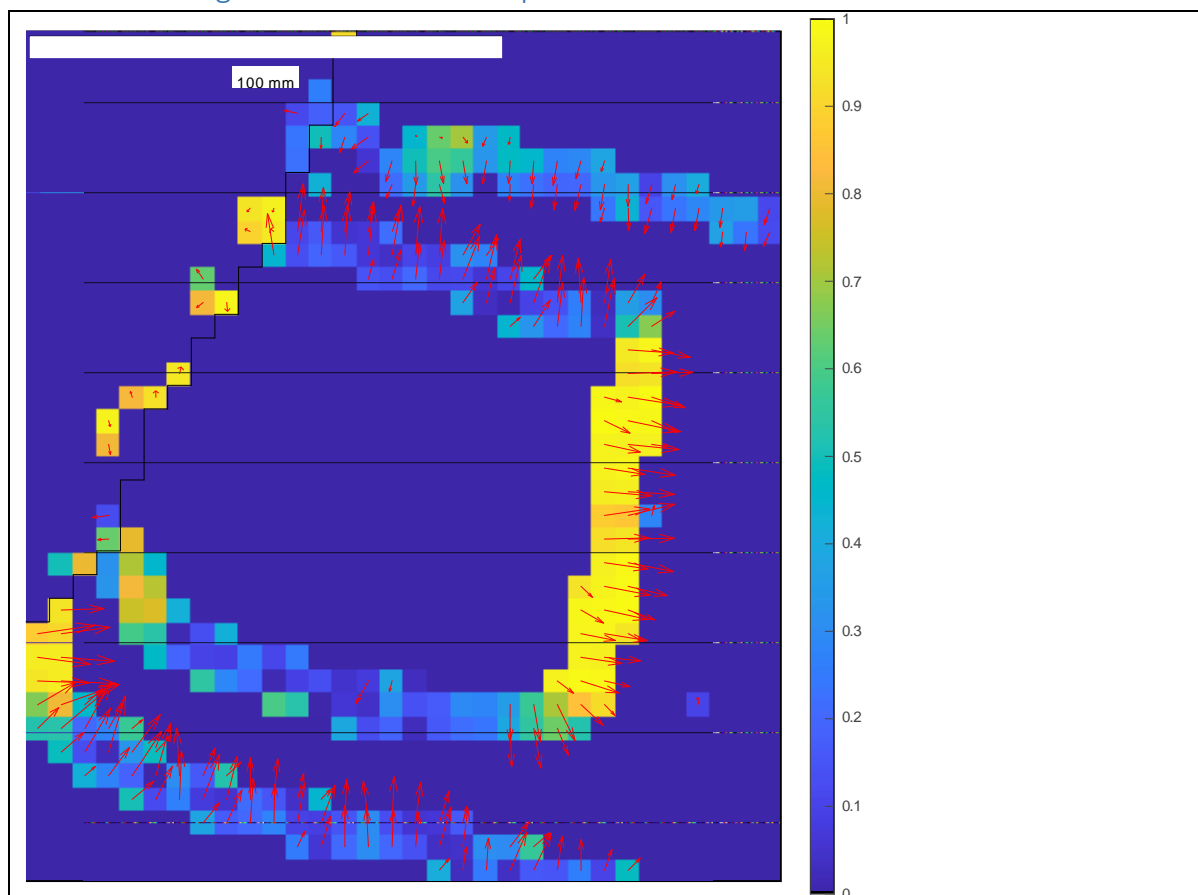


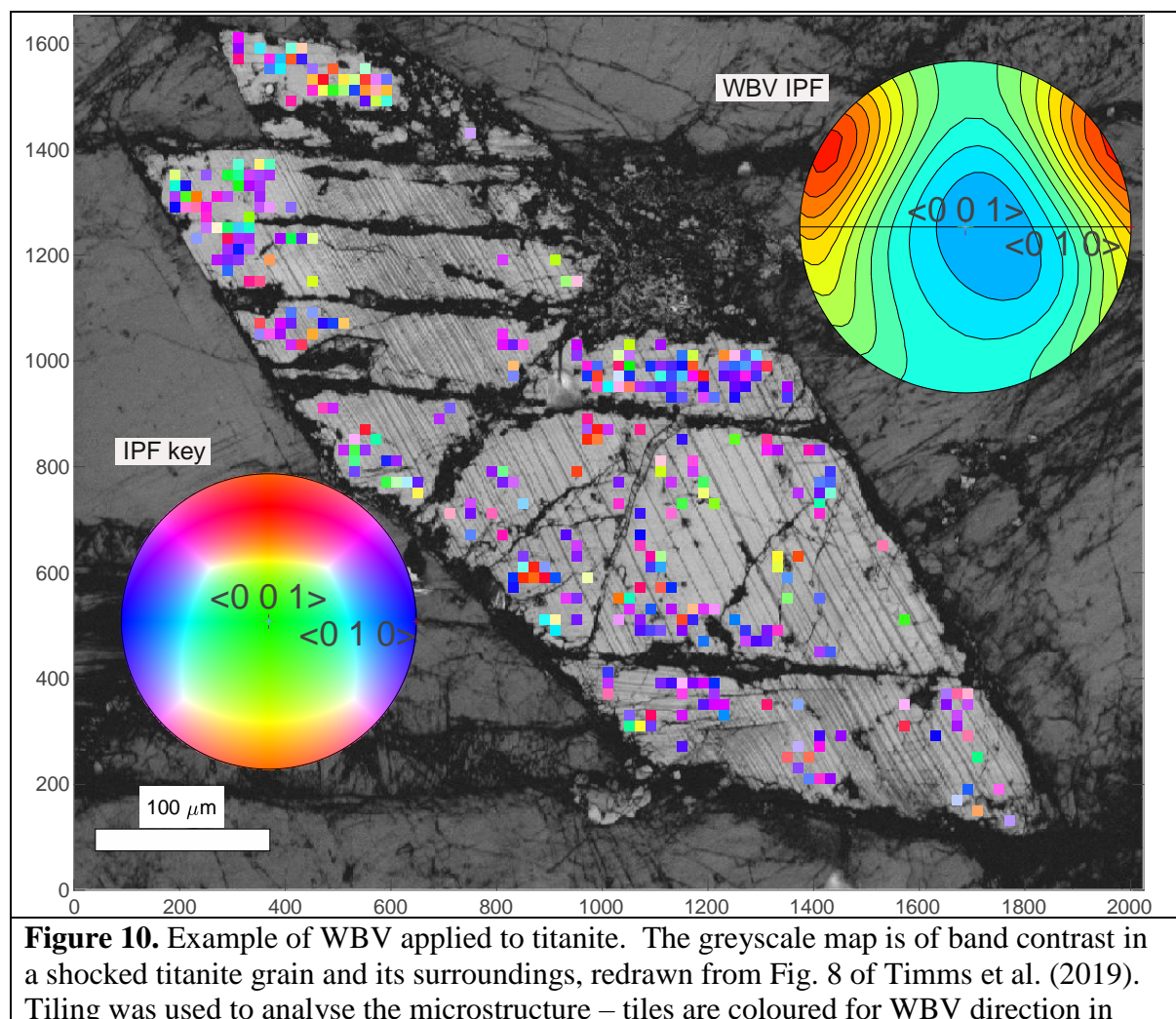
**Figure 9.** Example of WBV applied to a subgrain in ice, modified from Fig. 2 of Chauve et al. (2017). WBV is colour coded not by the full IPF but just by the sin of the angle of the WBV from the basal plane, i.e. (component of  $W$  parallel to  $c$ )/ $W$ . This runs between 0 and 1 as shown by the colour scale. Red arrows show the WBV projected onto the map plane, using its actual length not just its direction. Black line is a subgrain wall of  $5^\circ$  or more misorientation.

There is ongoing research into the role of non-basal slip in ice, since if that is active it will alter the rheology of ice sheets (Chauve et al., 2017; Piazzolo et al., 2015; Weikusat et al., 2011). Chauve et al. (2017) undertook deformation experiments on ice and Fig. 9a), modified from Fig. 2 of that paper, shows a subgrain from an experiment run at  $-7^\circ\text{C}$  and 0.5 MPa stress. The WBV is colour coded not by the full IPF but just by the sin of the angle of the WBV from the basal plane, i.e. (component of  $W$  parallel to  $c$ )/ $W$ . For this dataset we estimate  $\alpha_{95}$  as  $32^\circ$  (Table 1). The yellow vertical subgrain wall indicates angles near  $90^\circ$  from the basal plane so, even though the errors are large, there is negligible probability that these WBVs lie in the basal plane. Moreover, the colours along this wall are quite consistent, adding credence to the diagnosis that the WBV is subparallel to  $c$ . It does not immediately imply that individual Burgers vectors are parallel to  $c$ : for example, there could be a mixed population of  $c + a$  and  $c - a$ , bearing in mind the WBV is a vector average. Further data and/or assumptions are required to determine this. However, as noted above the WBV cannot contain “phantom” directions: it must be the weighted average of Burgers vectors that are actually present in the microstructure, and here must include non-basal vectors of some sort. The figure also provides an example of WBVs drawn in red as vectors in sample coordinates.

As discussed above and derived in Appendix 1, there is only one such choice at each point, regardless of crystal symmetry. Despite  $\alpha_{95}$  being predicted as  $32^\circ$ , the WBV directions along each wall segment are quite consistent, suggesting the angular errors are in fact lower, though further work is required to confirm this.

### 3.4. Titanite: discovery of new slip system

Fig. 10 shows the use of tiling in a study of deformed titanite, modified from Timms et al. (2019). The titanite grain is from a shocked granitoid from the Chicxulub impact structure, Mexico, and the study searched for slip systems activated under extreme stresses, which would not necessarily correspond to slip systems documented from other settings. The study included a boundary trace/misorientation approach, but that assumed pure tilt boundaries, so the WBV method was used for independent verification. The differential method gave a wide scatter of WBV directions so to reduce errors  $20 \times 20$  pixel tiles were used. The tiles are colour coded in terms of IPF direction; missing colours indicate either that the tile includes a high angle boundary, or the WBV magnitude is below the threshold for display (Table 1). There are many shock-induced twins, and the abundance of those high angle boundaries mean that tile coverage is sparse. However, the WBV directions show a strong maximum near  $\langle 341 \rangle$ . This is a Burgers vector not previously described in titanite but likely indicating a dislocation slip system operating concurrently with twinning under shock.



accordance with the IPF key on bottom left. The WBV IPF (top right) shows distinct preferred directions. Calculation and display parameters are given in Table 1.

### 3.5. WBV precision in specific studies

In Table 1 we compile the parameters required for estimating  $\alpha_{95}$  from previous studies making a big assumption, that the orientation measurement errors in those studies are all distributed uniformly between 0 and 0.01 radians. Despite this, the error estimates are in general agreement with the appearance of the relevant IPFs. For example, for Mg metal Fig. 5 shows IPFs with  $\alpha_{95}$  of  $28^\circ$  and  $14^\circ$ , and those angles are in accord with the scatters of points if all WBVs are in fact in the basal plane. One large  $\alpha_{95} = 110^\circ$  is for quartz and relates to Fig. 15 of Wheeler et al. (2009), but the left hand IPF there was drawn to specifically illustrate the effect of choosing a threshold  $W$  that is too low. The cone of error would cover the entire IPF and that is in accord with the random scatter of points seen. In contrast, another study is predicted to have a large  $\alpha_{95}$  of  $110^\circ$  yet the IPFs show strong maxima. Fig. 4 of Kendrick et al. (2017) shows IPFs of WBV for deformed plagioclase microlites in an andesite with strong maxima around [001], particularly in the experimentally deformed sample. We suggest this is because there is a single family of GNDs with a single [001] Burgers vector. Then, even though individual WBVs have large errors, the maximum is strong because the errors cancel out to some extent. This is analogous to a standard result in statistics of a single variable: the standard variation of the mean is equal to the standard deviation of an individual measurement divided by the square root of the sample size. A similar idea might be developed for directional statistics in future work.

## 4. Comparison of WBV with other methods used for analysing GND directional data

High resolution electron backscatter diffraction (HREBSD) is a technique which, in common with ours, aims at extracting useful information on GND densities and types from distorted crystals. To enable comparison, we provide here a simplified explanation of the method: for details see Wilkinson and Randman (2010), Wallis et al. (2016) and Wallis et al. (2019a). The name encompasses only part of the technique, which is based on two consecutive stages.

Stage 1. This stage involves a method aimed to determine very precise misorientations for small orientation differences. It is different to commercial EBSD analysis which is based on comparing orientation tensors derived from Hough transforms of Kikuchi patterns. In contrast, here the method of misorientation determination is based on direct comparison of Kikuchi patterns of adjacent analysis points. This gives very precise values for gradients in  $\mathbf{h}$  in the  $x$  and  $y$  directions (this is the High [Angular] Resolution part of the method). This is clearly beneficial for any calculation involving orientation gradients, but it comes at the cost of storing and transporting huge datasets, and of calculations which take days rather than minutes.

Stage 2. In the HREBSD method all 6 gradients are used to provide 6 constraints on the Nye curvature tensor. The method then uses a set of assumptions about dislocation types so as to solve a version of eqn (3) uniquely for dislocation densities e.g. Wilkinson and Randman (2010), Wallis et al. (2016). If there are 6 types of dislocation, then eqn (3) has a unique solution for 6 densities, given the 6 constraints on the Nye tensor. In many materials,

particularly cubic phases, symmetry indicates there are more than 6 types of slip system and there is no unique solution for eqn (3). So, an additional assumption is made: that the total line energy of all the dislocations involved is the minimum out of all the possible solutions.

The second stage calculations are based on three assumptions which we recommend deserve appraisal on a mineral-by-mineral basis.

i) We do not have a complete knowledge of all slip systems in all minerals, so making assumptions about them might be misleading.

ii) We need further information about the line energies of each type of dislocation to enable overall energy minimisation if there are more than 6 slip systems.

iii) Both methods analyse distortions, but these might be due to growth rather than deformation. In that case the concept of slip systems is not relevant: there might be alternative lists of allowable GND types, but again in minerals such information is scanty.

In contrast WBV calculation makes no assumptions about GND types at any stage of the calculations. Instead, individual studies tailor the interpretation, possibly involving further calculation, based on the problems being addressed. This is well illustrated in the published ice non-basal slip example outlined above. Here, the hypothesis to be tested was to identify if non-basal dislocations are present in ice. Hence, the user chose to calculate and display the angle of the WBV to the basal plane (Chauve et al., 2017). The calculation is free from detailed assumptions about dislocation types and energies, which are not well known. A further example is provided in Wieser et al. (2020) who used the trace of subgrain walls together with WBV analysis to provide additional constraints on potential activated slip systems. In this case, additional assumptions were introduced, e.g. that all subgrain walls were either pure tilt or pure twist. Those assumptions are not intrinsic to the WBV calculation. In essence the WBV provides a platform for further in depth analysis which may use additional assumptions.

Having defined the two stages in this discussion, note that in principle WBV could be used on Stage 1 HREBSD data, as in Wallis et al. (2016). Equally, best fit/energy minimisation can be used on Hough based orientation data as in Pantleon (2008). In the latter case, even though there must be significant orientation errors that propagate through the calculations, results can be informative if acquisition conditions are optimised for angular precision (Faul, 2021). An approach like that used here could provide information how errors propagate. In summary HREBSD, WBV and other methods for analysing dislocation density are all advantageous in different ways.

## 5. Summary and discussion

We have described the theoretical basis for the WBV method and shown examples where it has assisted in deducing Burgers vectors for slip systems in various minerals. Since the method is purely geometric it can also be used to analyse distortions due to growth as in Gardner et al. (2021). Key aspects of the WBV method are as follows.

- It makes no assumptions about the dislocation populations being investigated.
- It uses just the three numbers defining orientation at each measurement point, so is fast.
- It assumes there are no significant grain scale elastic strains.

The software we use in this contribution (“Crystalscape”) involves user-defined parameters for calculation as follows; these need to be recorded to allow calculations to be reproduced.

- The cutoff angle above which boundaries no longer have dislocation substructure, so should not be characterised using this method
- The size of the stencil or tile used for systematic calculations

WBV results can be displayed in several ways and the key user-defined parameters for display are the minimum and maximum WBV lengths. The minimum length can then, together with the other parameters, be used to estimate the angular accuracy  $\alpha_{95}$  (the shortest vectors being the least accurate in terms of direction). That estimation contains several simplifications and, in any case, depends on an assumed angular error in the EBSD data; but it serves as an indication of accuracy which proves useful.

For interpretation, the following properties must be borne in mind.

- The WBV does *not* measure the complete GND population or density. It is a sample of that population, weighted towards dislocation lines that intersect the EBSD map at high angles. Maps cut in different planes will show different but related WBV information.
- The WBV is a weighted sum of Burgers vectors of GNDs. In general, there are multiple ways of decomposing the WBV, but it still provides a platform for testing hypotheses. It will never generate “phantom” components. For example, if a trigonal or hexagonal mineral shows WBVs with significant c axis components, there must be GNDs with Burgers vectors involving c (though not necessarily parallel to c).
- Errors in WBV are smaller when larger stencils or tiles are used. Angular errors are smaller for longer WBVs.
- Larger stencils or tiles tend to “smear out” the WBV pattern. Increased angular precision is thus linked to reduced spatial resolution.

Future directions using this method could include further development of ways to characterise non-basal slip in hexagonal and trigonal materials e.g. Chauve et al. (2017). The combination of WBV analysis with subgrain boundary trace analysis (Wieser et al., 2020) has potential to be developed for olivine and other minerals. More advanced statistical tests related to directional data could be developed. We have not discussed 3D orientation data here but in principle this allows calculation of orientation gradients in all three dimensions and hence the complete Nye tensor which would be valuable for constraining GNDs. However, even the 9 components of the Nye tensor are not sufficient to constrain all GND types in very symmetric minerals. Statistical tests could be developed for 3D analysis as we have done in 2D. Hybrid approaches using two or more maps at right angles also deserve investigation.

We note that the methods discussed here are applicable to any crystalline material including metals, ceramics and ice.

## Acknowledgements

We thank all the user of the WBV method who have contributed through discussion to developing the technique.

## Data Availability Statement

In 2021 Oxford Instruments Nanoanalysis adapted a version of the WBV technique for use in Aztec Crystal, their EBSD analysis suite. This is described here:

<https://www.ebsd.com/ois-ebsd-system/dislocation-density-analysis> and in a webinar here

<https://register.gotowebinar.com/register/5472775566652982031>. In view of the commercial aspects, a Matlab version of the software used here (“Crystalscape”) is available from the lead author, for academic use only.

## Table 1. Details of published WBV studies, and the new studies here

Table 1. Published papers using WBV on minerals, with precision estimates added in this contribution. We include one example of use on Mg metal as it helps illustrate the basic ideas. In the right hand columns we have compiled information from the published works so as to estimate  $\alpha_{95}$ .

Crystal system	Laue group	Phase	Weighted Burgers Vector study motivation	Reference	Figure in referenced paper	Integral method used?	Stencil or tile	Sampled area (pixels)	Step size ( $\mu\text{m}$ )	W minimum length ( $(\mu\text{m})^{-1}$ )	$\alpha_{95}$ (deg)
Cubic holosymmetric	m3m	Periclase	example	(Wheeler et al., 2009)	Fig 11		s	9	10	0.0015	14.9
Cubic	m3		<i>no studies yet published on minerals</i>	-							-
Hexagonal holosymmetric	6/mmm	Mg	example	(Wheeler et al., 2009)	Fig 3, 5		s	9	4	0.002	28.1
		Mg	example	(Wheeler et al., 2009)			s	9	4	0.004	13.9
		Ti	magnitude display from TKD data	(Trimby et al., 2014)	Fig 5				0.01		n/a
		Ice	search for non-basal dislocations	(Piazolo et al., 2015)			s	9	15	0.0004	37.7
		Ice	search for non-basal dislocations	(Chauve et al., 2017)	Fig. 2		s	9	5	0.0014	32.2
Hexagonal	6/m		<i>no studies yet published on minerals</i>	-						-	
Trigonal holosymmetric	-3m	Quartz	example	(Wheeler et al., 2009)	Fig 15		s	9	2	0.001	110.0
		Quartz	example	(Wheeler et al., 2009)	Fig 15		s	9	2	0.003	37.7
		Quartz	compare GND density with density from etch pits	(Billia et al., 2013)	n/a	y					n/a
		Calcite	deduce slip systems hence deformation T	(Mcnamara et al., 2020)	Fig 4, 5						
Trigonal	-3		<i>no studies yet published on minerals</i>	-							
Tetragonal holosymmetric	4/mmm	Zircon	Link magnitude to Pb loss	(MacDonald et al., 2013)	Fig. 9	y			1, 2, 0.8		n/a
		Zircon	Planar deformation bands	(Kovaleva et al., 2015)	Fig. 6	y					n/a
		Zircon	help to characterise slip systems	(Kovaleva et al., 2018)	Fig. 6	y					n/a
Tetragonal	4/m		<i>no studies yet published on minerals</i>	-						-	
Orthorhombic	mmm	Olivine	confirm slip systems dominated by [100]	(Tielke et al., 2019)	Fig. 5 b	y	s	9	3	0.005	14.9
		Olivine	determine slip systems	(Wieser et al., 2020)	Fig. 4, 7						
		Olivine	tiling example	<i>this contribution</i>	Fig. 7	y	t	100	16	0.00005	26.2
		Olivine	stencil example	<i>this contribution</i>	Fig. 7		s	9	16	0.001	13.9
Monoclinic	2/m	Titanite	Diagnose slip systems: map showing WBV direction (6 $\mu\text{m}$ tiles)	(Timms et al., 2019)	Fig. 8c		t	400	0.3	0.001	24.6
		Titanite	Contoured IPF showing WBV direction (2.4 $\mu\text{m}$ tiles)	(Timms et al., 2019)	Fig. 8e		t	64	0.3	0.003	32.6
Triclinic	-1	Plagioclase	Diagnose slip system in naturally and experimentally deformed microlites; latter show [001] clearly; both show it in loops	(Kendrick et al., 2017)	Fig. 4		s	9	0.2	0.01	110.0
		Plagioclase	Understand plagioclase replacement by albite	(Gardner et al., 2021)	Fig. 6		s				
		Plagioclase	tiling example	<i>this contribution</i>	Fig. 8	y	t	400	1	0.0005	14.7
		Plagioclase	stencil example	<i>this contribution</i>	Fig. 8		s	21	1	0.01	9.5

## References

- Ashby, M. F. (1970), Deformation of plastically non-homogeneous materials, *Philosophical Magazine*, 21(170), 399-424, doi:10.1080/14786437008238426.
- Billia, M. A., N. E. Timms, V. G. Toy, R. D. Hart, and D. J. Prior (2013), Grain boundary dissolution porosity in quartzofeldspathic ultramylonites: Implications for permeability enhancement and weakening of mid-crustal shear zones, *Journal Of Structural Geology*, 53, 2-14, doi:10.1016/j.jsg.2013.05.004.
- Butler, R. F. (1992), *Paleomagnetism: Magnetic Domains to Geologic Terranes*, Blackwell Scientific Publications.
- Chauve, T., M. Montagnat, S. Piaolo, B. Journaux, J. Wheeler, F. Barou, D. Mainprice, and A. Tommasi (2017), Non-basal dislocations should be accounted for in simulating ice mass flow, *Earth And Planetary Science Letters*, 473, 247-255, doi:10.1016/j.epsl.2017.06.020.
- De Graef, M. (2020), A dictionary indexing approach for EBSD, *IOP Conference Series: Materials Science and Engineering*, 891, 012009, doi:10.1088/1757-899x/891/1/012009.
- Drury, M. R., and J. L. Urai (1990), Deformation related recrystallization processes, *Tectonophysics*, 172, 235-253.
- Faul, U. (2021), Dislocation structure of deformed olivine single crystals from conventional EBSD maps, *Physics and Chemistry of Minerals*, 48(9), 35, doi:10.1007/s00269-021-01157-3.
- Gardner, J., J. Wheeler, and E. Mariani (2021), Interactions between deformation and dissolution-precipitation reactions in feldspar at greenschist facies, *Lithos*, 396-397.
- Gardner, R. L., S. Piaolo, N. R. Daczko, and P. Trimby (2020), Microstructures reveal multistage melt present strain localisation in mid-ocean gabbros, *Lithos*, 366, doi:10.1016/j.lithos.2020.105572.
- Hildyard, R. C., D. J. Prior, D. R. Faulkner, and E. Mariani (2009), Microstructural analysis of anhydrite rocks from the Triassic Evaporites, Umbria-Marche Apennines, Central Italy: An insight into deformation mechanisms and possible slip systems, *Journal Of Structural Geology*, 31(1), 92-103, doi:10.1016/j.jsg.2008.10.009.
- Jiang, J., T. B. Britton, and A. J. Wilkinson (2013), Measurement of geometrically necessary dislocation density with high resolution electron backscatter diffraction: Effects of detector binning and step size, *Ultramicroscopy*, 125, 1-9, doi:10.1016/j.ultramic.2012.11.003.
- Kalácska, S., Z. Dankházi, G. Zilahi, X. Maeder, J. Michler, P. D. Ispánovity, and I. Groma (2020), Investigation of geometrically necessary dislocation structures in compressed Cu micropillars by 3-dimensional HR-EBSD, *Materials Science and Engineering: A*, 770, 138499, doi:<https://doi.org/10.1016/j.msea.2019.138499>.
- Kendrick, J. E., Y. Lavalley, E. Mariani, D. B. Dingwell, J. Wheeler, and N. R. Varley (2017), Crystal plasticity as a strain marker of the viscous-brittle transition in magmas, *Nature Communications*, 8(1), Art. No. 1926, doi:10.1038/s41467-017-01931-4.
- Konijnenberg, P. J., S. Zaefferer, and D. Raabe (2015), Assessment of geometrically necessary dislocation levels derived by 3D EBSD, *Acta Materialia*, 99, 402-414, doi:10.1016/j.actamat.2015.06.051.
- Kovaleva, E., U. Klotzli, G. Habler, and J. Wheeler (2015), Planar microstructures in zircon from paleo-seismic zones, *American Mineralogist*, doi:10.2138/am-2015-5236.

- Kovaleva, E., U. Klotzli, J. Wheeler, and G. Habler (2018), Mechanisms of strain accommodation in plastically-deformed zircon under simple shear deformation conditions during amphibolite-facies metamorphism, *Journal Of Structural Geology*, 107, 12-24, doi:10.1016/j.jsg.2017.11.015.
- Lloyd, G. E. (2002), Microstructural evolution in a mylonitic quartz simple shear zone: the significant roles of dauphine twinning and misorientation, paper presented at Joint International Meeting of the Tectonic-Studies-Group of the Geological-Society London/Structural Geology and Tectonics Division of the Geological-Society-of-America/Geological-Society-of-Australia, London, ENGLAND, Sep 02-03.
- Lopez-Sanchez, M. A., A. Tommasi, W. Ben Ismail, and F. Barou (2021), Dynamic recrystallization by subgrain rotation in olivine revealed by electron backscatter diffraction, *Tectonophysics*, 815, doi:10.1016/j.tecto.2021.228916.
- MacDonald, J. M., J. Wheeler, S. L. Harley, E. Mariani, K. M. Goodenough, Q. G. Crowley, and D. Tatham (2013), Lattice distortion in a zircon population and its effects on trace element mobility and U–Th–Pb isotope systematics: examples from the Lewisian Gneiss Complex, northwest Scotland, *Contributions To Mineralogy And Petrology*, 166, 21-41, doi:10.1007/s00410-013-0863-8.
- Mcnamara, D. D., A. Lister, D. J. Prior, A. Scully, J. Gardner, and J. Wheeler (2020), Microanalysis of Calcite Scaling in a Fractured Geothermal System.
- Nicolay, A., J. M. Franchet, J. Cormier, H. Mansour, M. De Graef, A. Seret, and N. Bozzolo (2019), Discrimination of dynamically and post-dynamically recrystallized grains based on EBSD data: application to Inconel 718, *JOURNAL OF MICROSCOPY*, 273(2), 135-147, doi:10.1111/jmi.12769.
- Nye, J. F. (1953), Some geometrical relations in dislocated crystals, *Acta Metallurgica*, 1, 153-162.
- Pantleon, W. (2008), Resolving the geometrically necessary dislocation content by conventional electron backscattering diffraction, *Scripta Materialia*, 58(11), 994-997, doi:10.1016/j.scriptamat.2008.01.050.
- Piazolo, S., M. Montagnat, F. Grennerat, H. Moulinec, and J. Wheeler (2015), Effect of local stress heterogeneities on dislocation fields: Examples from transient creep in polycrystalline ice, *Acta Materialia*, 90, 303-309, doi:10.1016/j.actamat.2015.02.046.
- Prior, D. J. (1999), Problems in determining the orientations of crystal misorientation axes, for small angular misorientations, using electron backscatter diffraction in the SEM, *Journal of Microscopy*, 195, 217-225.
- Prior, D. J., E. Mariani, and J. Wheeler (2009), EBSD in the Earth Sciences: applications, common practice and challenges, in *Electron Backscatter Diffraction in Materials Science*, edited by A. J. Schwartz, M. Kumar, B. L. Adams and D. P. Field, pp. 345-357, Springer.
- Ram, F., S. Zaefferer, T. Japel, and D. Raabe (2015), Error analysis of the crystal orientations and disorientations obtained by the classical electron backscatter diffraction technique, *Journal of Applied Crystallography*, 48(3), 797-813, doi:doi:10.1107/S1600576715005762.
- Spruzeniece, L., S. Piazolo, and H. E. Maynard-Casely (2017), Deformation-resembling microstructure created by fluid-mediated dissolution-precipitation reactions, *Nature Communications*, 8, doi:10.1038/ncomms14032.
- Tielke, J. A., J. Mecklenburgh, E. Mariani, and J. Wheeler (2019), The influence of water on the strength of olivine dislocation slip systems, *Journal Of Geophysical Research: Solid Earth*, 124, 6542-6559, doi:10.1029/2019JB017436.

- Tielke, J. A., M. E. Zimmerman, and D. L. Kohlstedt (2017), Hydrolytic weakening in olivine single crystals, *Journal of Geophysical Research-Solid Earth*, 122(5), 3465-3479, doi:10.1002/2017jb014004.
- Timms, N. E., et al. (2019), New shock microstructures in titanite (CaTiSiO<sub>5</sub>) from the peak ring of the Chicxulub impact structure, Mexico, *Contributions To Mineralogy And Petrology*, doi:<https://doi.org/10.1007/s00410-019-1565-7>.
- Timms, N. E., S. M. Reddy, D. Healy, A. A. Nemchin, M. L. Grange, R. T. Pidgeon, and R. Hart (2012), Resolution of impact-related microstructures in lunar zircon: A shock-deformation mechanism map, *Meteoritics & Planetary Science*, 47(1), 120-141, doi:10.1111/j.1945-5100.2011.01316.x.
- Trimby, P. W., et al. (2014), Characterizing deformed ultrafine-grained and nanocrystalline materials using transmission Kikuchi diffraction in a scanning electron microscope, *Acta Materialia*, 62, 69-80, doi:<http://dx.doi.org/10.1016/j.actamat.2013.09.026>.
- Wallis, D., L. N. Hansen, T. Ben Britton, and A. J. Wilkinson (2016), Geometrically necessary dislocation densities in olivine obtained using high-angular resolution electron backscatter diffraction, *Ultramicroscopy*, 168, 34-45, doi:10.1016/j.ultramic.2016.06.002.
- Wallis, D., L. N. Hansen, T. B. Britton, and A. J. Wilkinson (2019a), High-Angular Resolution Electron Backscatter Diffraction as a New Tool for Mapping Lattice Distortion in Geological Minerals, *Journal of Geophysical Research: Solid Earth*, 0xx, xxx, doi:10.1029/2019jb017867.
- Wallis, D., A. J. Parsons, and L. N. Hansen (2019b), Quantifying geometrically necessary dislocations in quartz using HR-EBSD: Application to chessboard subgrain boundaries, *Journal of Structural Geology*, 125, 235-247, doi:10.1016/j.jsg.2017.12.012.
- Weikusat, I., A. Miyamoto, S. H. Faria, S. Kipfstuhl, N. Azuma, and T. Hondoh (2011), Subgrain boundaries in Antarctic ice quantified by X-ray Laue diffraction, *J. Glaciol.*, 57(201), 111-120.
- Wheeler, J., E. Mariani, S. Piazzolo, D. J. Prior, P. Trimby, and M. R. Drury (2009), The Weighted Burgers Vector: a new quantity for constraining dislocation densities and types using Electron Backscatter Diffraction on 2D sections through crystalline materials, *Journal of Microscopy*, 233(3), 482-494, doi:10.1111/j.1365-2818.2009.03136.x.
- Wieser, P., M. Edmonds, J. MacLennan, and J. Wheeler (2020), The Record of Magma Storage under Kīlauea Volcano preserved in Distorted Olivine Crystals, *Nature Communications*, doi:10.1038/s41467-019-13635-y.
- Wilkinson, A. J., and D. Randman (2010), Determination of elastic strain fields and geometrically necessary dislocation distributions near nanoindentations using electron back scatter diffraction, *Philosophical Magazine*, 90(9), 1159-1177, doi:10.1080/14786430903304145.

## References for the Supporting Information

- Humphreys, F. J., P. S. Bate, and P. J. Hurley (2001), Orientation averaging of electron backscattered diffraction data, *Journal of Microscopy*, 201, 50-58.
- Watson, G. S. (1982), Distributions on the Circle and Sphere, in *Essays in Statistical Science*, edited by J. Gani and E. J. Hannan, pp. 265-280.
- Wheeler, J., E. Mariani, S. Piazzolo, D. J. Prior, P. Trimby, and M. R. Drury (2009), The Weighted Burgers Vector: a new quantity for constraining dislocation densities and

types using Electron Backscatter Diffraction on 2D sections through crystalline materials, *Journal of Microscopy*, 233(3), 482-494, doi:10.1111/j.1365-2818.2009.03136.x.

Wheeler, J., D. J. Prior, Z. Jiang, R. Spiess, and P. J. Trimby (2001), The petrological significance of misorientations between grains, *Contributions to Mineralogy and Petrology*, 141, 109-124, doi:10.1007/s004100000225.



*Journal of Geophysical Research – Solid Earth*

Supporting Information for

**Using crystal lattice distortion data for geological investigations: the Weighted Burgers Vector method**

J. Wheeler<sup>1</sup>, S. Piazzolo<sup>2</sup>, D. J. Prior<sup>3</sup>, P. W. Trimby<sup>4</sup> and J. A. Tielke<sup>5</sup>

<sup>1</sup>Department of Earth, Ocean, and Ecological Sciences, University of Liverpool, 4 Brownlow Street, Liverpool, L69 3GP, UK

<sup>2</sup>University of Leeds, School of Earth & Environment, Leeds LS2 9JT, UK

<sup>3</sup>Department of Geology, University of Otago, Dunedin, New Zealand

<sup>4</sup>Oxford Instruments Nanoanalysis, High Wycombe, Bucks, England

<sup>5</sup>Lamont-Doherty Earth Observatory of Columbia University, Palisades, NY, USA

**Contents of this file**

Three Appendices describing mathematical background to WBV and error analysis, table of notation and captions to two supplementary figures

**Additional Supporting Information (Files uploaded separately)**

Wheeler et al. Supplementary Figures S1 and S2 as jpg files

## Appendix 1: WBV, numerical aspects and symmetry

We briefly reiterate and extend here the maths in Wheeler *et al.* (2009); for notation see Table S1. We write some equations using vector notation for brevity though we find that index notation (including Einstein summation convention) is most generally useful. We use Greek and Latin indices for sample and crystal coordinate systems respectively otherwise confusion can easily result. For second rank and higher tensors, either can be used, or a “mixed” space. A fundamental concept is the orientation tensor  $\mathbf{h}$  which relates a vector  $\mathbf{C}$  in Cartesian crystal coordinates to its equivalent  $\mathbf{V}$  in sample coordinates

$$V_\gamma = h_{\alpha i} C_i$$

In what follows we assume that there are no elastic strains on the grain scale.

### 1.1. Differential method

Considering  $\mathbf{h}$  is a mathematical function of position the Nye tensor is defined by

$$\alpha_{i\gamma} = e_{\alpha\beta\gamma} h_{\alpha i, \beta} = \sum_N \rho^{(N)} b_i^{(N)} l_\gamma^{(N)} \quad (\text{A1.1})$$

where  $\mathbf{e}$  is the permutation tensor. If we know only the x and y gradients of  $\mathbf{h}$ , we can still determine 3 out of the 9 components of the Nye tensor

$$W_i = \alpha_{i3} = e_{\alpha\beta 3} h_{\alpha i, \beta} = h_{1i, 2} - h_{2i, 1} = \sum_N \rho^{(N)} b_i^{(N)} l_3^{(N)} = \sum_N \left[ \rho^{(N)} l_3^{(N)} \right] b_i^{(N)} \quad (\text{A1.2})$$

The vector  $\mathbf{W}$  encapsulates some but not all of the GND content: the term in square brackets indicates it is weighted towards dislocations lines at a high angle to the map.

EBSD measurements and hence  $\mathbf{h}$  values are determined at a finite number of spaced points. Thus, we must differentiate  $\mathbf{h}$  numerically. For example, to evaluate

$$h_{2i, 1} = \partial h_{2i} / \partial x$$

we could choose

$$(h_{2i}(x + u, y) - h_{2i}(x, y)) / u$$

where  $u$  is step size, or, more symmetrically,

$$(h_{2i}(x + u, y) - h_{2i}(x - u, y)) / (2u)$$

Because we are differentiating, we call this “differential” method.

The algorithm requires a minimum of 3 points to get gradients in both x and y (e.g. Fig. 4a)). However, this asymmetric pattern may give biased results, so Fig. 4b)-d) show some more symmetric patterns of nearby points which can be involved in the calculation. Such patterns, used for numerical differentiation in other contexts, are called “stencils”. In detail our differential method calculates a “best fit” lattice curvature to the misorientations at each point in the stencil. When high angle boundaries pass through the stencil, the points beyond the boundary are excluded from the fitting. This means that only a subset of the points in the stencil are used. Our “edge preserving” method differs somewhat from that of Humphreys *et al.* (2001).

Crystal symmetry must be accounted for in the calculation. When Kikuchi patterns are indexed, the procedure will give one orientation tensor  $\mathbf{h}$  from each pattern. Because of crystal symmetry there is a choice of  $\mathbf{h}$  values, related by symmetry, all equally valid. Adjacent points which are actually close in orientation may be indexed with different symmetry choices, giving very different numerical  $\mathbf{h}$  components and Euler angles. Numerical differentiation would then give huge and artificial orientation gradients so, rather than calculate gradients directly, the misorientations between points are calculated. The misorientation angle (strictly, “disorientation”) is defined as the *minimum* angle needed to rotate one orientation into another (Wheeler *et al.*, 2001), and the misorientation tensors generated are then used to calculate orientation gradients.

### 1.2. Integral method

Again considering  $\mathbf{h}$  is a mathematical function of position, evaluate the integral of  $\mathbf{h}$  around a closed loop on the map, followed anticlockwise. This gives the *net* WBV of GNDs whose lines cross through that loop, in units of length.

$$B_i = -\oint_{\text{antici}} h_{ai} dx_\alpha$$

We generally report the calculation after dividing the net WBV by loop area A, hence delivering a vector  $\mathbf{B}/A$  with units of  $(\text{length})^{-1}$ . Mathematically the differential and integral methods are precisely equivalent (they are related by a tensor version of Stokes’ theorem).

$$B_i = \int W_i dA$$

So  $\mathbf{B}/A$  is just the average value of  $\mathbf{W}$  inside the loop.

The numerical version of the integration is written as follows. For a square grid of points, we assume that a particular orientation measurement  $h_{ai}^{(p)}$  applies to a square region around the point p at which it was taken. In numerical integration, then, the “dx” term becomes a vector  $x_\alpha^{(p)}$  spanning this square region, horizontally, vertically, or diagonally (at corners). Then:

$$B_i = -\sum_{p=1}^L h_{ai}^{(p)} x_\alpha^{(p)}$$

where L is the number of points included in the loop.

### 1.3. Symmetry

When a crystal has symmetry, there is more than one choice for the orientation tensor  $\mathbf{h}$ . If  $\mathbf{h}$  is a valid description, then so is  $\mathbf{h}\mathbf{S}$  where  $\mathbf{S}$  is any symmetry operator expressed in crystal coordinates. Because  $\mathbf{h}$  is non-unique, so is  $\alpha_{i\gamma}$  and so is the WBV in crystal coordinates: hence it is plotted on the usual IPF segment. However, we now show that if the first index is transformed to sample coordinates, the tensor is unique. In sample coordinates

$$\alpha'_{\delta\gamma} = h_{\delta i} e_{\alpha\beta\gamma} h_{ai,\beta}$$

Let us replace  $\mathbf{h}$  by the symmetric equivalent  $\mathbf{h}\mathbf{S}$ , so then  $\alpha'$  becomes

$$\alpha'_{\delta\gamma} = h_{\delta p} S_{pi} e_{\alpha\beta\gamma} (h_{\alpha q} S_{qi})_{,\beta} = S_{pi} S_{qi} h_{\delta p} e_{\alpha\beta\gamma} h_{\alpha q,\beta} = h_{\delta i} e_{\alpha\beta\gamma} h_{ai,\beta} \quad (\text{A1.3})$$

because  $\mathbf{S}$  is a rotation tensor and so  $S_{pi}S_{qi}$  is the identity tensor. So  $\alpha'$  has a unique value when both coefficients are in sample coordinates, and so does the WBV.

## Appendix 2: Derivations of model Nye tensors

Since we have chosen olivine as our example mineral, we have designed models so that distortion can be expressed by GNDs with [100] and [001] vectors. The distortions are gradational but we use the same nomenclature as that for subgrain walls.

### 2.1. Tilt

Our tilt model is in essence 2D - there are no distortions in the 3<sup>rd</sup> dimension – so we begin with a completely general 2D model in which lattice orientation is defined by a single angle as a function of position  $\theta(x, y)$ , with anticlockwise rotation positive. Then the orientation tensor is

$$h_{\alpha i} = \begin{pmatrix} \cos \theta & -\sin \theta & 0 \\ \sin \theta & \cos \theta & 0 \\ 0 & 0 & 1 \end{pmatrix}$$

So

$$h_{\alpha i, \beta} = q_{\alpha i} \theta_{, \beta}$$

where

$$q_{\alpha i} = \begin{pmatrix} -\sin \theta & -\cos \theta & 0 \\ \cos \theta & -\sin \theta & 0 \\ 0 & 0 & 0 \end{pmatrix}$$

From eqn (A1.1) we obtain, considering the zero values in  $\mathbf{e}$  and  $\mathbf{q}$

$$\alpha_{i\gamma} = e_{\alpha 1\gamma} q_{\alpha i} + e_{\alpha 2\gamma} q_{\alpha i} \theta_{,2} = e_{21\gamma} q_{2i} \theta_{,1} + e_{12\gamma} q_{1i} \theta_{,2}$$

So setting  $\gamma = 3$  the WBV is, in crystal coordinates

$$\mathbf{W} = (-\cos \theta \theta_{,1} - \sin \theta \theta_{,2}, \sin \theta \theta_{,1} - \cos \theta \theta_{,2}, 0)$$

and in sample coordinates

$$\mathbf{W} = -(\theta_{,1} \theta_{,2}, 0)$$

This simple result tells us that orientation variations in the x direction relate to Burgers vectors with an x component (in sample coordinates) and similarly for y: a rigorous version of what we discussed in the introduction.

Now we design a specific 2D model: a tilted crystal so that rotations are around [001], perpendicular to the map, and [010] is parallel to rays from the centre of curvature. Then, let x and y in map view be measured relative to the centre of curvature, r be the distance from the centre so the misorientation of [100] relative to the x axis is:

$$\theta = -\text{atan}\left(\frac{x}{y}\right)$$

so the gradient vector is

$$\theta_{, \beta} = \frac{1}{r}(-\cos \theta, -\sin \theta, 0)$$

so in sample coordinates

$$\mathbf{W} = \frac{1}{r}(\cos \theta, \sin \theta, 0) \quad (\text{A2.1})$$

And in crystal coordinates

$$\mathbf{W} = \frac{1}{r}(1, 0, 0)$$

## 2.2. Twist

Misorientation is around the [010] axis, running parallel to x. Let the misorientation relative to the y axis be an arbitrary function of x. This allows us to deal with a linear function (constant distortion) or a quadratic function (increasing distortion)

$$\theta = \theta(x)$$

and

$$h_{\alpha i} = \begin{pmatrix} 0 & -1 & 0 \\ \cos \theta & 0 & \sin \theta \\ -\sin \theta & 0 & \cos \theta \end{pmatrix}$$

So

$$h_{\alpha i, \beta} = q_{\alpha i} \theta_{, \beta}$$

where

$$q_{\alpha i} = \begin{pmatrix} 0 & 0 & 0 \\ -\sin \theta & 0 & \cos \theta \\ -\cos \theta & 0 & -\sin \theta \end{pmatrix}$$

And the gradient vector

$$\theta_{, \beta} = \left( \frac{d\theta}{dx}, 0, 0 \right)$$

From eqn (A1.1) we obtain

$$\begin{aligned} \alpha_{i\gamma} &= e_{\alpha 1\gamma} q_{\alpha i} \theta_{, 1} = e_{21\gamma} q_{2i} \theta_{, 1} + e_{31\gamma} q_{3i} \theta_{, 1} \\ &= \frac{d\theta}{dx} \begin{pmatrix} 0 & -\cos \theta & \sin \theta \\ 0 & 0 & 0 \\ 0 & -\sin \theta & -\cos \theta \end{pmatrix} \end{aligned}$$

and in crystal coordinates (setting  $\gamma = 3$ )

$$\mathbf{W} = \frac{d\theta}{dx}(\sin \theta, 0, -\cos \theta) \quad (\text{A2.2})$$

To transform  $\mathbf{W}$  sample coordinates, calculate  $\mathbf{hW}$  to find

$$\mathbf{W} = \frac{d\theta}{dx}(0, 0, -1) .$$

So in sample coordinates the WBV ( $= \alpha_{\beta 3}$ ) is a vector parallel to z.

## Appendix 3: Error analysis

### 3.1. Standard deviation of WBV

We undertook numerical modelling to assess how errors in orientation measurements propagate. To generate figures S1 and S2, we took the two models of Fig. 2 and added orientation errors by imposing small additional rotations. Each additional rotation matrix was generated using a unit vector rotation axis selected at random, and a rotation angle selected at random from the range 0 to 0.01 rad. We then calculated the WBV using various methods. The calculations are undertaken in sample coordinates, meaning the theoretical and calculated WBVs have unique values as shown in eqn. (A1.3). and implying that crystal symmetry does not enter into the calculations. For that reason, although the models are for olivine, we assert that the results will apply in any crystal system, because we are applying equations which do not involve symmetry operations. For display we find IPFs are easier to understand even though calculations are undertaken in sample coordinates.

*First row.* Fig. S1 a)-c) show IPFs for three different stencil sizes, and d)-f) for three different tile sizes. The noise has led to larger scatter in WBV direction for small stencils and tiles.

*Second row.* To understand this in more detail, we compare the theoretical WBV of eqn (A2.1), denoted here as  $\mathbf{W}_c$ , with the calculated WBV, defining an error vector  $\mathbf{E}$  as the difference between the two. Fig. S1 g)-i) show the magnitudes of the error vectors (blue cloud) for three stencil sizes. Errors do not seem to be correlated with WBV size and to quantify this, we must use the statistics of vectors. Any error vector  $\mathbf{E}$  has a covariance matrix given by

$$C_{ij} = \text{mean}(E_i E_j)$$

We find that the covariance, a second rank tensor, is somewhat anisotropic in our models but rather than consider that detailed complexity, we assume isotropy

$$\mathbf{C} = \frac{1}{3}\sigma^2\mathbf{I},$$

where  $\mathbf{I}$  is the identity tensor, and then

$$\sigma^2 = \text{trace}(\mathbf{C}) = \text{mean}(E_1^2 + E_2^2 + E_3^2)$$

Here  $\sigma$  can be thought of as a standard deviation for the vector  $\mathbf{E}$ . We calculated it for the entire  $W$  range, and also for binned intervals of  $W$  to discover whether  $W$  had a strong effect on  $\sigma$ . For each particular model, e.g. Fig S1g), the cyan line shows the average values of  $\sigma$  in bins of width 0.002. We do not see a strong correlation with  $W$  (bearing in mind the vagaries of such numerical experiments) so we propose that  $\sigma$  should be considered independent of  $W$ . In contrast,  $\sigma$  clearly decreases from g) to i) so the idea that larger stencils will reduce directional errors is confirmed. Although directional errors are reduced, the larger stencil size means that a larger region of microstructure is contributing to the calculation, so it is less obvious where the contributing GNDs are. In Fig. S1j)-l) we repeat this analysis for tiles of different sizes.

*Third row.* In Fig. S1m)-r) we display the angular errors. The magenta lines indicate the points below which 95% of the data lie (for binned ranges of  $W$ ). The red lines are discussed below.

In Fig. S2 we show the same error analysis for a smooth twist structure as in Fig. 2, using the theoretical WBV given by eqn. (A2.2). The same patterns in error are shown: again, the magnitude of the error vector is not dependent on  $W$ , so the angular error is less for larger  $W$ ; again, larger stencil sizes give smaller errors.

These graphs are not intended as a universal guide as to how orientation measurement errors will affect WBV directional errors, because many different types of 3D orientation gradients may exist, but they serve as a preliminary indication. We quantify the link between standard deviation of  $W$  with dimensionless stencil size  $S$  or tile size  $T$ . For each of the 12 models (6 tilt, 6 twist) we calculate the value of  $\sigma$  across the entire range of  $W$  (in essence averaging the values shown by the blue lines). We then did a best fit of  $\log \sigma$  versus  $\log S$  or  $\log T$ , finding an exponent of -0.99 for stencils and -0.718 for tiles. An outline algebraic analysis under development for tiles suggests the exponent is -3/4; for stencils we rounded it to -1. A best fit using these exponents then gives:

$$\sigma_S = 0.0247S^{-1}/u \quad (\text{A3.1})$$

where  $u$  is step size, and with the dimensionless area  $T$  of a tile:

$$\sigma_T = 0.0081T^{-3/4}/u. \quad (\text{A3.2})$$

### 3.2. Angular errors from standard deviations

To link these standard deviations to directional statistics we assume a Fisher distribution in which the directions are distributed in accordance with a probability density function  $F$

$$F = \frac{\kappa}{4\pi \sinh \kappa} \exp(\kappa \cos \psi)$$

where  $\psi$  is the angle from the mean direction, and  $\kappa$  is known as a ‘‘concentration’’ parameter (Watson, 1982). When  $\kappa$  is large the distribution is very focussed around the mean direction and that would be expected to relate to small values of standard deviation  $\sigma$  of  $\mathbf{W}$ . To quantify that, we refer to section 2 of (Watson, 1982) and note that the definition of  $\sigma$  there is equal to our definition divided by  $\sqrt{3}$ . Watson defines a parameter  $m = W\sqrt{3}/\sigma$  (in our notation) and then shows how it relates to  $\kappa$  via his eqn. (30). Having  $\kappa$  we calculate the 95% confidence angle by integrating  $F$  to obtain the proportion of the distribution within an angle  $\theta$ , and then rearranging to find the angle within which 95% of the distribution lies:

$$\alpha_{95} = \text{acos} \left( 1 + \frac{1}{\kappa} \ln(1 - 0.95(1 - \exp(-2\kappa))) \right)$$

To help to understand the errors, this equation can be related back to the inset cartoons in Fig. 4. When  $\kappa$  is large and errors are small

$$\begin{aligned} \alpha_{95} &\cong \text{acos} \left( 1 + \frac{1}{\kappa} \ln(0.05) \right) \cong \text{acos} \left( 1 + \frac{1}{m^2} \ln(0.05) \right) \cong \frac{1}{m} \sqrt{2 \ln(20)} \\ &= \frac{\sigma}{W} \sqrt{2 \ln(20)/3} = 1.413 \frac{\sigma}{W} \end{aligned}$$

where we have used the Watson eqn. 30 for large  $\kappa$  and the power series expansion of  $\cos$ . Although there is now a constant of proportionality, the basic link between vector and directional errors in Fig. 4 is confirmed. For binned ranges of  $W$ , we plot the calculated

values of  $\alpha_{95}$  as red lines in the bottom rows of Figs. S1 and S2. These are comparable to the magenta lines which are calculated directly from the model data (particularly for the twist models), suggesting that our statistical analysis is adequate. We note our models are based on “noise” up to 0.01 radian. We expect that eqns (A3.1) and (A3.2) will scale with the level of noise but assessing angular noise levels is not a straightforward procedure and is a topic for future research.

### 3.3. Angular errors and crystal symmetry

Our calculation of  $\alpha_{95}$  does not consider crystal symmetry. The error cone should be the same in crystal coordinates but there are some subtleties to consider. If  $\alpha_{95}$  was for example  $3^\circ$  then this could help specify a narrow cone of directions, displayed as a small circle, within which the true direction lay on a PF or an IPF. However, if  $\alpha_{95}$  was  $40^\circ$  in, for example, the cubic crystal system, then the error cone would overlap several symmetric equivalents and be difficult to interpret; it might cover most of the IPF. In general, the error cone would be sliced up by symmetry operations and would be represented by several small circle arcs on an IPF; it is beyond the scope of this contribution to consider this in detail. Nevertheless, we find our estimates of  $\alpha_{95}$  are always informative.

### 3.4 Summary

In summary, and adding practical detail, errors are evaluated as follows. In bold are the quantities which enter into the calculation.

1. Assume a particular range of orientation **measurement errors** in the EBSD measurements (we give an example where we assume errors go up to 0.01 rad).
2. We use a particular **stencil or tile area** for WBV calculation and calculate the standard deviation in  $W$  from eqn (A3.1) and (A3.2) which also requires the **step size**.
3. To get an overview of errors in WBV PFs and IPFs when looking at a range of WBVs, we want the maximum relevant  $\alpha_{95}$  so we select a **minimum WBV length** which then allows calculation of  $m$ , then  $\kappa$ , then  $\alpha_{95}$ .

Supplementary Table S1. Notation.

Symbol	Meaning	Units, if dimensional
A	Area of integration loop on map	(length) <sup>2</sup>
<b>B</b>	Net Burgers vector sum for dislocations threading a particular loop	length
<b>e</b>	Permutation tensor (3 <sup>rd</sup> rank)	-
<b>h</b>	Orientation tensor (2 <sup>nd</sup> rank)	-
K <sub>i</sub>	i <sup>th</sup> coefficient for writing <b>W</b> in terms of lattice basis vectors	(length) <sup>-2</sup>
<b>L</b> <sub>i</sub>	i <sup>th</sup> lattice basis vector	length
S	Area of stencil in pixels	-
T	Area of tile in pixels	-
<b>W</b>	Weighted Burgers Vector	(length) <sup>-1</sup>
W	Magnitude of <b>W</b>	(length) <sup>-1</sup>
W <sub>t</sub>	Characteristic W used in precision analysis	(length) <sup>-1</sup>
W <sub>c</sub>	Theoretical value of <b>W</b> in noise-free model	(length) <sup>-1</sup>
<b>E</b>	Error vector in value of <b>W</b> in noisy model = <b>W</b> – W <sub>c</sub>	(length) <sup>-1</sup>
ρ <sup>(N)</sup>	Density of N <sup>th</sup> type of dislocation	(length) <sup>-2</sup>
<b>b</b> <sup>(N)</sup>	Burgers vector of N <sup>th</sup> type of dislocation	length
<b>l</b> <sup>(N)</sup>	Unit line vector of N <sup>th</sup> type of dislocation	-
u	Step size	length
X, y, z	Cartesian coordinate system	length
α <sub>95</sub>	Angle related to precision of a direction. 95% chance that the true direction of a vector is that angle or less from the calculated direction	-
<b>α</b>	Nye Curvature tensor (2 <sup>nd</sup> rank)	(length) <sup>-1</sup>
<b>κ</b>	Curvature tensor (2 <sup>nd</sup> rank)	(length) <sup>-1</sup>
κ	“concentration” parameter in spherical statistics (Appendix 3)	-
σ	“Standard deviation” of a vector, assuming isotropic covariance (Appendix 2)	Same as vector
σ <sub>S</sub>	Standard deviation of <b>W</b> when calculated using stencils	(length) <sup>-1</sup>
σ <sub>T</sub>	Standard deviation of <b>W</b> when calculated using tiles	(length) <sup>-1</sup>

## Captions for supplementary figures

**Figure S1.** Analysis of errors in the noisy tilt model.

a)-f) For the noisy model, IPF plots for WBV calculated for three stencil sizes (left) and three tile sizes (right) with a  $W$  threshold of  $0.001 \text{ } (\mu\text{m})^{-1}$ .

g)-l) Errors (magnitude of  $\mathbf{W}_e$ ) versus  $W$  for the various stencils and tiles in a). In each graph, individual values are plotted as a blue cloud and the cyan line indicates the average value of error for binned ranges of  $W$ .

m)-r) Directional errors (angle between  $\mathbf{W}$  and  $\mathbf{W}_c$ ) versus  $W$  for the various stencils and tiles as in upper rows. In each graph, individual values are plotted as a blue cloud and the magenta line indicates the points below which 95% of the data lie (for binned ranges of  $W$ ). The red line indicates predicted  $\alpha_{95}$ . The  $W$  minimum thresholds used in displays in a) are shown by stars.

**Figure S2.** Analysis of errors in the noisy twist model, organised as in Fig. S1.